Energy & Environmental Science

REVIEW

View Article Online
View Journal | View Issue

Cite this: *Energy Environ. Sci.*, 2016, **9**, 1190

Two-dimensional layered MoS_2: rational design, properties and electrochemical applications†

Gong Zhang,[ab] Huijuan Liu,*[a] Jiuhui Qu[a] and Jinghong Li*[c]

Received 14th December 2015,
Accepted 1st February 2016

DOI: 10.1039/c5ee03761a

www.rsc.org/ees

The layered molybdenum chalcogenide MoS_2 has attracted wide attention due to its potential electrochemical applications. Based on its unique physical and chemical properties, numerous advances have shown that nanostructured MoS_2, with the advantages of low cost and outstanding properties, is a promising candidate for environmentally benign energy conversion and storage (ECS) devices. Nowadays, in order to lessen the reliance on fossil fuels, the production of hydrogen from water splitting has become an important issue. Hence, developing catalysts composed of earth-abundant elements that possess activities comparable to those of noble metals is of great urgency. According to DFT calculations in terms of HER free-energy diagrams, MoS_2 could be used as an effective substitute for noble metals. Meanwhile, MoS_2 with various structures has also been applied in the field of energy storage, including batteries and supercapacitors. Additionally, due to their layer-dependent electrical properties, MoS_2-based electrochemical devices have been applied as sensors for a variety of chemicals. In this review, we summarize recent advances in the development of MoS_2 with high-performance in various electrochemical domains, and recent progress in discovering the mechanisms underlying the enhanced activity. Moreover, we summarize the critical obstacles facing MoS_2, and discuss strategies for further improving its activity. Lastly, we offer some suggestions on the pathways toward achieving high performance competitive with noble metal counterparts, and perspectives on practical applications of MoS_2 in the future.

Broader context

The development of inexhaustible and clean energy technologies has far-reaching benefits for our society. Owing to its high anisotropy and unique crystal structure, the attractive properties of 2D molybdenum disulfide (MoS_2) can be utilized in a variety of energy conversion and storage (ECS) applications. Therefore, understanding how these properties can be tuned and the tunable properties can be utilized becomes increasingly important. In this review, we first summarize recent synthetic strategies toward preparation of MoS_2 with different structures, and its role in several important renewable energy technologies. We then discuss the relationship between the tuned properties and the performance of MoS_2 in different applications, emerging trends during their development, and challenges facing them, offering our perspectives on how to effectively advance the development of MoS_2-based devices.

1. Introduction

The production of energy is currently the most important issue for society. Development of inexhaustible and clean energy technologies will have far-reaching long-term benefits. It will increase countries' energy security *via* reliance on an indigenous and inexhaustible resource, and thereby enhance sustainability and reduce pollution. Thus, it is of great significance to develop highly efficient and environmentally benign energy conversion and storage (ECS) devices, including fuel cells,[1,2] solar cells,[3] water-splitting cells,[4,5] batteries[6,7] and supercapacitors.[8] The performance of these devices depends on the properties of the materials used. Therefore, breakthroughs in the field of nanomaterial chemistry are believed to be pivotal to the development of highly efficient ECS devices.

Molybdenum disulfide (MoS_2), a type of layered transition-metal dichalcogenide, has been widely applied in the field of catalysis[9] and as a material in ECS devices, such as batteries,[10] photovoltaics,[11] and electronic transistors.[12] The transition metals have different numbers of d-electrons, filling up d bands

[a] *Key Laboratory of Drinking Water Science and Technology, Research Center for Eco-Environmental Sciences, Chinese Academy of Sciences, Beijing 100085, China. E-mail: hjliu@rcees.ac.cn*
[b] *University of Chinese Academy of Sciences, Beijing 100039, China*
[c] *Department of Chemistry, Beijing Key Laboratory for Microanalytical Methods and Instrumentation, Tsinghua University, Beijing 100084, China. E-mail: jhli@mail.tsinghua.edu.cn*

† Electronic supplementary information (ESI) available. See DOI: 10.1039/c5ee03761a

to different levels, resulting in varying electronic properties.[13,14] This range of properties make possible the development of MoS_2 electronic and optoelectronic devices, and the applications of MoS_2 in catalysis.[15] In MoS_2 crystals, layers of Mo in a hexagonal array are sandwiched between S layers. Strong covalent bonding characterizes the Mo–S interactions, while the interactions between S layers are van der Waals interactions along the *z* axis to form the bulk material. Due to its high anisotropy and unique crystal structure, the properties of 2D MoS_2 can be tuned *via* reducing dimensions, intercalation, and formation of heterostructures.[16]

As a well-known hydro-desulfurization catalyst,[17] MoS_2 has been considered as an ideal catalyst for the electrocatalytic hydrogen evolution reaction (HER) according to computational and experimental studies.[18] Hydrogen, an ideal energy carrier, plays a significant role in future technologies.[19,20] The DFT calculations in terms of the HER free-energy diagram predict that only the S–Mo–S edges in MoS_2 sheets are active for hydrogen atom adsorption, and the [1010] Mo edges are mainly responsible for bringing about a favorable free energy change for hydrogen atom adsorption, which is very close to that observed on state-of-the-art Pt surfaces.[21] Therefore, increasing the number of active edge sites in MoS_2 by modifying the atomic structure, or by changing the electronic structure of the system to increase the enthalpy of hydrogen adsorption, or by incorporating the sheets into conducting nano- or micro-sized templates has remained an important issue for efficient hydrogen production.[22–28] In addition, energy storage is another important technological and scientific problem that has global implications for humanity. MoS_2, with a capacity three and half times higher than that of commercial graphite anodes (372 mA h g^{-1}),[29] is becoming the subject of significant attention as a battery anode material. Generally, compared to other materials, MoS_2 displays much better capability and its lower rates of cycling induced degradation,[30] and the less volumetric expansion upon lithiation is an attractive advantage. Moreover, 2D MoS_2-based structures have also been widely applied in many other domains (Scheme 1), such as photocatalysis,[31,32] sensing,[33–36] and dielectric applications.[37]

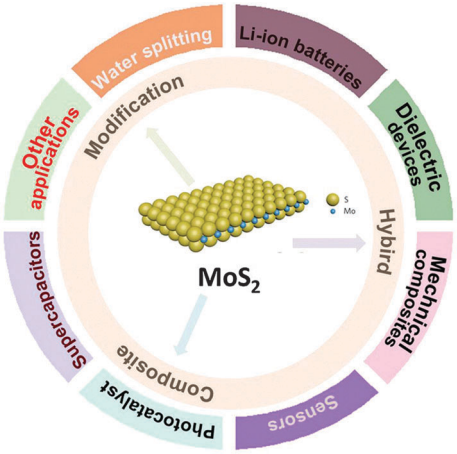

Scheme 1 Illustration of the nanostructured MoS_2 materials and their potential applications in various domains.

Gong Zhang

Gong Zhang received his BSc degree at Hohai University in 2012. He is now supervised by Prof. Huijuan Liu and focuses on the synthesis of nanomaterials for photo- and electro-catalytic applications.

Huijuan Liu

Huijuan Liu received her PhD degree from the Chinese Academy of Sciences (2003) (CAS, 2003). She is now a full professor of the Research Center for Eco-Environmental Sciences, CAS and received the China Young Scientist Award in 2013. Her research interests are the water purifying principle and technology of adsorption, coagulation, photo- and electro-chemical processes.

Jinghong Li

Jinghong Li is a Cheung Kong Professor in the Department of Chemistry at Tsinghua University, China. He received his BSc in 1991 from the University of Science and Technology of China and his PhD in 1996 from the Changchun Institute of Applied Chemistry, Chinese Academy of Sciences. His current research interests include electro-analytical chemistry, bio-electrochemistry and sensors, physical electrochemistry and interfacial electrochemistry, electrochemical materials science and nanoscopic electrochemistry, fundamental aspects of energy conversion and storage, advanced battery materials, and photoelectrochemistry.

Although there are already a number of excellent reviews on the attractive properties of MoS_2, understanding how these properties can be tuned and the tunable properties can be utilized becomes increasingly important. In this review, we first summarize the recent synthetic strategies towards preparation of MoS_2 with different nanostructures. Then, the tuning of MoS_2 structures through physical and chemical methods and optimization of properties are focused on. Following that, the relationships between the tuned properties and the performance of MoS_2 in different applications are elucidated. Finally, a perspective on major challenges and opportunities facing MoS_2 materials will be proposed.

2. Preparation methods for MoS_2

In order to enhance desired properties, the selection of an effective fabrication method should be the first and pivotal step. Numerous methods have been employed to prepare MoS_2, in order to optimize its properties and achieve the superior performance. Examples of materials prepared from a top-down approach have been based on the exfoliation of bulk MoS_2,[38–40] such as mechanical cleavage, chemical intercalation followed by exfoliation,[41–43] liquid phase exfoliation by direct sonication, and laser thinning techniques.[44] Meanwhile, examples of bottom-up approaches are CVD growth and chemical synthesis.[45–47]

2.1 Top-down methods

MoS_2 nanosheets containing tens to hundreds of crystal 2D layers can be achieved *via* mechanical cleavage from the bulk MoS_2. Novoselov *et al.* successfully applied this method to prepare single-layer MoS_2 from the bulk.[48] After a fresh surface of a layered bulk crystal was rubbed against a Si/SiO_2 surface, flakes with various thicknesses of MoS_2 were detached and adsorbed onto the target surface. Single-layer MoS_2 sheets could be further obtained from the thicker flakes, which was confirmed by scanning electron microscopy (SEM). The mechanical cleavage for the preparation of nanosheets has been applied to obtain pristine 2D MoS_2 with high quality (Fig. 1A). Meanwhile, the as-obtained nanosheets can be utilized for the study of the properties and fabrication of electronic devices.[49–51]

Although mechanical cleavage can produce 2D MoS_2 with high quality, low throughput limits this method in practical applications. To obtain the large quantities of single-layer MoS_2 sheets, the solution based exfoliation methods are often used. Recently, some research groups have developed chemical or electrochemical Li-intercalation and exfoliation intercalation methods to produce MoS_2 nanosheets.[19,52] In order to ameliorate the experimental conditions necessary for the chemical Li-intercalation (high temperature or long reaction time), an electrochemical Li-intercalation method was developed (Fig. 1B). The process was utilized in a Li-ion battery configuration comprised by using bulk MoS_2 as the cathode and lithium foil as the anode. In this system, the amount of inserted lithium can be adjusted by the discharge curve, leading to effective Li-insertion,

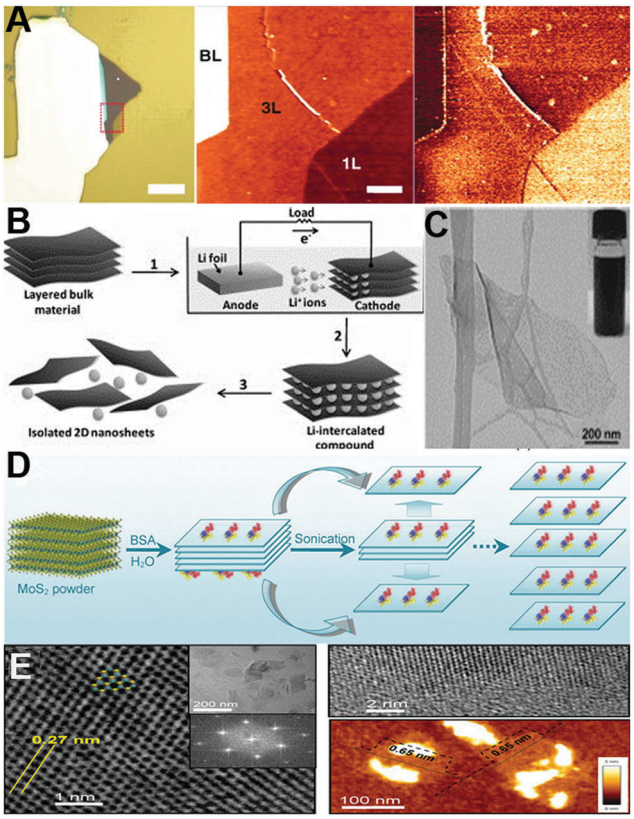

Fig. 1 (A) Bright-field optical microscopy images (left) of thin sample flakes, and the red dotted squares represent the subsequent AFM scan areas. Scale bars, 10 μm. Copyright 2010, the American Association for the Advancement of Science. (B) Electrochemical lithiation process for the fabrication of 2D nanosheets from the layered bulk material, and (C) TEM image of a typical MoS_2 nanosheet. Inset: Photograph of MoS_2 solution. Copyright 2011, John Wiley and Sons. (D) Schematic for the BSA-induced exfoliation of single-layer MoS_2 nanosheets under sonication, and (E) TEM images of the single-layer MoS_2 nanosheet at the center and the edge. The insets are the corresponding low-resolution TEM image and the fast Fourier transform pattern. Copyright 2015, American Chemical Society.

thereby achieving the sufficient Li-intercalation. After discharge, Li_xMoS_2 was sonicated in water or ethanol. The reaction between lithium and solution generated H_2 gas, which exfoliated MoS_2 layers effectively. Under agitation, well-dispersed MoS_2 nanosheets were finally obtained (Fig. 1C).

For reliable and scaled-up production of atomically thin MoS_2 nanosheets, some studies demonstrated that the exfoliation process can be achieved by sonicating the bulk in various liquid phases, such as *N*-methylpyrrolidone,[53] dimethyl-formamide,[44,54] or a mixture of ethanol and water.[55] These liquid phases can not only exfoliate MoS_2 but also stabilize the nanosheets to some given extent due to their effect on the surface energy. In addition, liquid-phase exfoliation has been extended to the application of surfactant-containing solutions.[56] Accordingly, these methods hold great promise for scaled-up production of layered MoS_2 in environmentally benign solutions. Recently, by using bovine serum albumin (BSA) as an exfoliating agent, Guan and his coworkers demonstrated a layer-by-layer exfoliation route to produce layered MoS_2 nanosheets with high yield in aqueous

solution (Fig. 1D).[57] In contrast to earlier liquid-phase exfoliation methods, single-layer nanosheets with high dispersion were achieved due to the strong binding of BSA (Fig. 1E). Due to the strong binding of the chemical ligands in solutions, the chemical exfoliations produced highly dispersed single-layer MoS_2 nanosheets, which provide the significance platform to study some deep-seated properties and thereby exploiting the novel applications.

2.2 Bottom-up approach

Because of the violent nature of the chemical exfoliation, the crystal structure becomes deformed. However, large-area MoS_2 with mono- or several-layer structures can be prepared by using the chemical vapor deposition (CVD) method. Compared with chemical exfoliation, the CVD method is more efficient in growing MoS_2 monolayer films on substrates (SiO_2/Si[58] or Au[59]), with high quality and controllable thickness.[44,60] Moreover, the formation of the continuous MoS_2 films by CVD is compatible with the current electronic fabrication processes, making this a promising candidate for building atomically thin layered electrical,[61] photovoltaic,[62] optical[63] or HER[19] devices.

A two-step thermolysis process was recently reported for deposition of ultrathin MoS_2 nanosheets by dip-coating of ammonium thiomolybdates on Si/SiO_2 foils and converting the films to MoS_2 by annealing at 500 °C followed by sulfurization at 1000 °C under sulfur vapor (Fig. 2A). The chemical reaction resulted in the formation of MoS_2 layers. The second step at 1000 °C was required to enhance the crystallinity. Typically, MoO_3 and sulfur powders are used as precursors for deposition of MoS_2 films on acetone and isopropanol-cleaned Si/SiO_2 foils. Upon heating, the reaction of volatile suboxides (MoO_{3-x}) with the sulfur vapor gave MoS_2 layers on the substrate. Using refined CVD, crystalline islands of monolayer molybdenum disulphide with high carrier mobility were grown up to 120 μm lateral size, which had the potential to provide superior optical or electrical properties to those of exfoliated samples.[61] Moreover, some deep insights into the relationship between the lattice orientation, edge morphology and crystallinity and island shape were also provided by transmission electron microscopy. To obtain MoS_2 with high conductivity, Shi *et al.* also selected MoO_3 and sulfur powders as precursors for deposition of MoS_2 films on Au foils by the low pressure chemical vapor deposition (LPCVD) method (Fig. 2B).[64]

Continuous films of MoS_2 samples, containing single- to few-layers, with tunable lateral sizes can be obtained. The sample can be transferred onto substrates like SiO_2/Si and quartz for a variety of applications. In consideration of its characteristics of atomic flatness and hexagonally arranged in-plane lattice, mica would be a suitable substrate for the growth of materials with the same symmetry. The lattice symmetry of mica well-matched with MoS_2, so that epitaxial growth monolayer MoS_2 could be predicted. Accordingly, Ji *et al.* have applied the LPCVD process to controllably synthesize centimeter-scale uniform monolayer MoS_2 on one type of mica ($KMg_3AlSi_3O_{10}F_2$).[58] In addition to the use of various substrates, other researchers have explored different Mo and S precursors as an effective pathway for the fabrication of MoS_2 with better properties, such as direct deposition of sulfur vapor onto the Mo film.[65] The size and thickness of the Mo film determined the size and thickness of the resulting MoS_2 film, making this synthesis process highly scalable.

Meanwhile, wet chemical synthesis is another common bottom-up method for preparing MoS_2, *e.g.*, hydrothermal and solvothermal reactions.[24,66–70] Typically, $(NH_4)_6Mo_7O_{24}{\cdot}4H_2O$ and thiourea have been utilized as the precursors for the Mo and S elements in hydrothermal reactions. After reaction in a Teflon-lined stainless steel autoclave, the low-quality MoS_2 flakes with abundant active sites are obtained (Fig. 2C). These visible internal edges (tears, pinholes and defects) benefit its electrocatalysis performance.

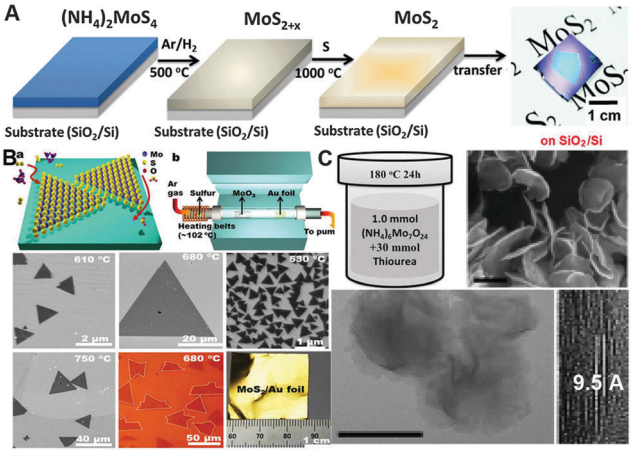

Fig. 2 (A) Schematic illustration of the two-step thermolysis process for the synthesis of MoS_2 thin layers on insulating substrates. The precursor $(NH_4)_2MoS_4$ was dip-coated on SiO_2/Si or sapphire substrates followed by a two-step annealing process. The as-grown MoS_2 film can be transferred onto other arbitrary substrates.[71] Copyright 2011, American Chemical Society. (B) LPCVD synthesis of monolayer MoS_2 on Au foils: schematic view of the surface growth of MoS_2 on Au foils, and the experimental setup. SEM images show the triangular MoS_2 flakes grown at different growth temperatures displaying different domain sizes. The optical microscopy image shows the as-grown MoS_2 on Au foils with more complicated shapes, and the diagram illustrates a possible batch production process. Copyright 2014, American Chemical Society. (C) Schematic illustration of the fabrication of MoS_2 *via* the hydrothermal method: SEM and HRTEM images of the defect-rich MoS_2 ultrathin nanosheets. Copyright 2013, American Chemical Society.

3. Properties of MoS_2

3.1 Crystal properties

Naturally, MoS_2 can form a phase with trigonal prismatic or an octahedral Mo coordination. 2H and 3R MoS_2 both correspond to trigonal prismatic coordination.[72,73] The 2H type, which is dominant and more stable in nature, has two layers per unit cell stacked in the hexagonal symmetry. The 3R-type has three layers per cell in rhombohedral symmetry, and is unstable and easily transforms to 2H upon heating. In most studies, MoS_2

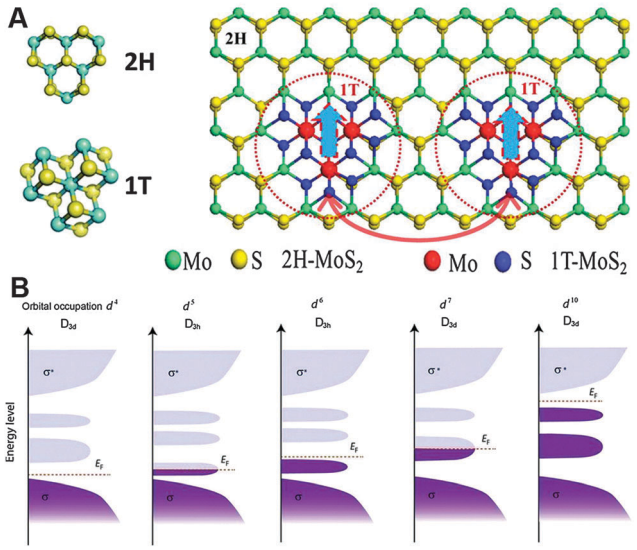

Fig. 3 (A) The 2H and 1T phase of MoS_2, and diagrammatic representation of the phase incorporation of the 1T phase in 2H-MoS_2 nanosheets. (B) Qualitative schematic illustration showing progressive filling of d orbitals that are located within the bandgap of bonding (σ) and anti-bonding states (σ*) in group 4, 5, 6, 7 and 10 TMDs. D_{3h} and D_{3d} refer to the point groups associated with the trigonal prismatic and octahedral coordination of the transition metals. When an orbital is partially filled (such as in the case of group 5 and 7 TMDs), the Fermi level (E_F) is within the band and the compound exhibits a metallic character. When an orbital is fully filled (such as in group 6 TMDs), the Fermi level is in the energy gap and a semiconducting character is observed. Copyright 2015, American Chemical Society.

with 2H crystal structure has been used as a precursor to prepare mono- or few-layer MoS_2 nanosheets. Meanwhile, the shift of one of the sulfur layers leads to an AbC stacking sequence, resulting in the generation of the 1T crystal phase, which has trigonal symmetry and corresponds to octahedral coordination of the metal atoms (Fig. 3A).

Generally, the filling of Mo d orbitals is directly influenced by the structure of MoS_2. For the trigonal prismatic phase (2H), the d orbital splits into three degenerate states with an energy gap of 1 eV, while the d orbitals degenerate into other forms of orbitals in the tetragonal symmetry of the 1T phase, and up to six electrons can fill the e_{2g} orbital.[74] As shown in Fig. 3B, because the p orbitals of sulfur are at much lower energy than the Fermi level, the filling of d orbitals determines the nature of the different phases in MoS_2 compounds. Complete filling of orbitals gives rise to semiconducting behavior (2H) while partial filling results in metallic behavior (1T).[75] Thus, as orbital occupation varies, the electronic properties of MoS_2 gradually change from metal, to semiconductor, to topological insulator, and this provides a diversity of physical and chemical properties for a wide variety of applications.

In solid materials, phase transitions can be used to change the properties without adding additional atoms and are therefore of significant technological value, thereby the properties can be further extended. In contrast to the 2D MoS_2 nanosheets obtained from mechanical exfoliation, the coexistence of the metallic and semiconducting phases has been reported in chemically exfoliated MoS_2 by Eda and colleagues.[76] By combining the results of X-ray photoelectron spectroscopy (XPS) and scanning TEM (STEM), mixtures of 2H and 1T phases in single-layer MoS_2 were identified (Fig. 4A). Furthermore, the dynamic process of the transformation between 2H and 1T phases involving intra-layer atomic plane gliding has been experimentally proven by

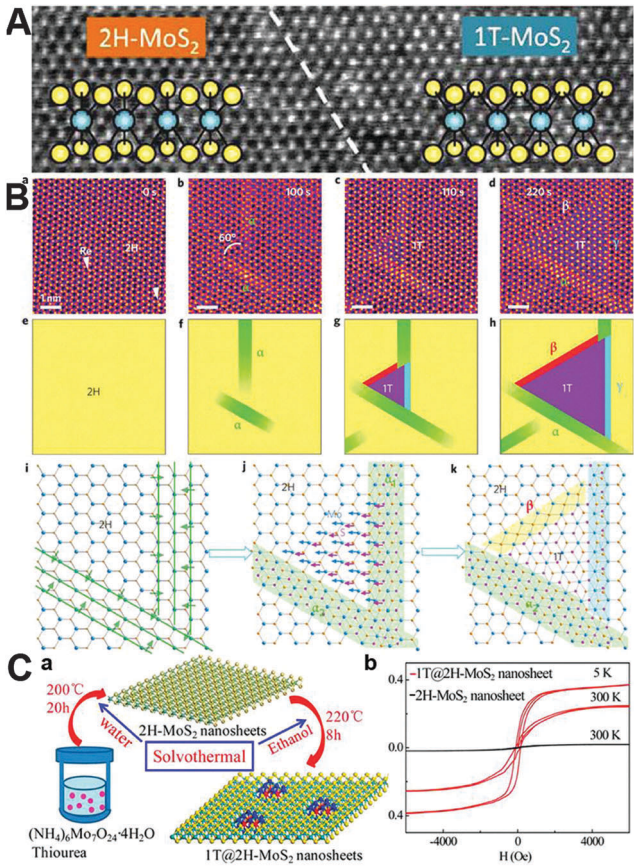

Fig. 4 (A) STEM image of a region where a boundary between 2H (left) and 1T (right) phases is observed. The phase boundary is parallel to [−1100] planes and marked by a dashed line. Copyright 2012, American Chemical Society. (B) (a) Single-layered MoS_2 doped with Re substitution dopants (indicated by arrowheads) has the initial 2H phase of a hexagonal lattice structure with a clear HC. (b) At t = 100 s, two identical intermediate (precursor) phases (denoted α) form with an angle of 60°, and consist of three constricted Mo zigzag chains. (c) At t = 110 s, a triangular shape indicating the 1T phase (~1.08 nm^2) appears at the acute corner between the two α-phases. (d) At t = 220 s, the area of the transformed 1T phase is enlarged to ~8.47 nm^2. Three different boundaries (α, β and γ) are found at the three edges between the 1T and 2H phases. (e–h) Simple schematic illustrations of the 2H right arrow 1T phase transition corresponding to the ADF images in a–d, respectively. (i) Atomic model of α-phase formation by the constriction of three Mo zigzag chains. (j) Nucleation of the 1T phase (triangular) with the Mo + S (or S′) atoms gliding in the directions indicated by blue and pink arrows. (k) β-Boundary formation at the growth frontier side. The α1-phase transforms to a γ-boundary, and the α_2-phase becomes wider. Copyright 2014, Macmillan Publishers. (C) (a) Schematic representation of the two-step hydrothermal synthetic route for the 1T@2H-MoS_2 nanosheets and magnetization *vs.* magnetic field (M–H) curves at 5 and 300 K (b). Copyright 2015, American Chemical Society.

using an aberration-corrected STEM.[77] The dynamic process of the atomic motions was visualized in the single-layered MoS_2. In addition to the glide of the sulfur plane, the phase transformation in the MoS_2 sheet involves atomic displacements (Fig. 4B). The atomic process of phase transitions involves 2H–1T, 1T–2H, 2H–2H′ and 1T–1T′ phase transitions, and the transitions are composed of three elemental steps: (i) formation of the α-phase as a precursor or an intermediate state, and (ii and iii) migration of the β and γ boundaries.

MoS_2 samples with mixture 2H/1T phases can also be achieved *via* a facile chemical reaction,[19,69] and the synergistic effect of the metallic and semiconducting properties can be utilized. The 1T phase was reported to be formed by transformation of 2H-MoS_2 by Li and K intercalation.[78] In addition, a strategy for the incorporation of the 1T phase into the 2H phase was recently reported involving a two-step wet chemical synthesis (Fig. 4C). After introduction of sulfur vacancies in the 2H-MoS_2 nanosheet host during the solvothermal reaction, the transformation of the surrounding 2H-MoS_2 local lattice into a trigonal (1T) phase was prompted. The result not only induces robust room-temperature ferromagnetism in a nonmagnetic form of MoS_2, but also enhances the electron carrier concentration by an order of magnitude.

3.2 Electronic and optical structures

The band structures of MoS_2 materials can be calculated based on density functional theory (DFT). When the bulk is reduced to a single layer, it had been predicted that an indirect to direct bandgap transition would occur in the d-electron system. Bulk MoS_2 is an indirect-gap semiconductor having a bandgap of about 1 eV, with a valence band maximum (VBM) at the *Γ* point and a conduction band minimum (CBM) at the mid-point along *Γ*–*K* symmetry lines (Fig. 5A), while the monolayer form is a direct-gap semiconductor with VBM and CBM coinciding at the *K*-point.[79] Splendiani *et al.* reported on the thickness-dependent physical properties of MoS_2.[80] Combined with optical absorption, photoluminescence (PL), and photoconductivity, the evolution of electronic structure and the resulting optical properties of ultrathin MoS_2 crystals were observed as a function of the number of layer numbers. The crossover from an indirect gap material to a direct gap material accounted for the enhancement of luminescence in the MoS_2 monolayer. The observed dependence of the bandgap on the layer number was in agreement with band calculations. Furthermore, the bandgap transition was derived from quantum confinement effects, resulting in pronounced differences in the emissions from photo-excitation in the bulk and monolayer material. As depicted in Fig. 5C, the bulk showed negligible photoluminescence, while thinner exhibited much stronger PL signals.[81,82]

Raman scattering is ultrasensitive to the number of layers in these materials. Thus, Raman spectroscopy serves as an essential tool for studying the structure and electronic properties of 2D MoS_2. Theoretical calculations predicted four first-order Raman active modes for crystalline MoS_2.[83] The E^2_g mode, an interlayer mode, with a Raman shift at 32 cm^{-1} is derived from the

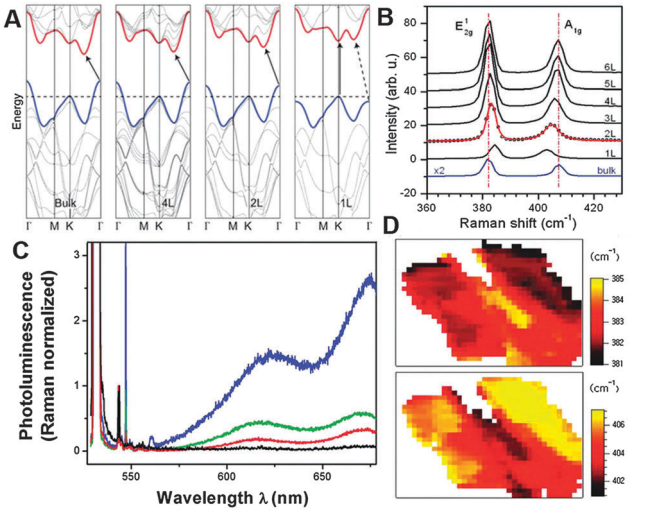

Fig. 5 (A) Energy dispersion (energy *versus* wavevector k) in bulk, quadrilayer (4L), bilayer (2L) and monolayer (1L) MoS_2 from left to right. The horizontal dashed line represents the energy of a band maximum at the K point. (B) Photoluminescence spectra normalized by Raman intensity for MoS_2 layers with different thicknesses, showing a dramatic increase of luminescence efficiency in the MoS_2 monolayer. Copyright 2010, American Chemical Society. (C) Raman spectra of thin and bulk MoS_2 films. The solid line for the 2L spectrum is a double Voigt fit of the data (circles for 2L and solid lines for the rest). (D) Spatial maps of the Raman frequency of E^1_{2g} and A_{1g} modes for the sample. Copyright 2010, American Chemical Society.

vibration of two rigid layers. The other three Raman active modes were mainly induced by the intralayer atomic vibrations. In contrast to the in-plane vibration modes (E_{1g} or E^1_g), the A_1 mode is an out-of-plane vibration mode. Lee *et al.* applied Raman scattering for the MoS_2 nanosheets with various thicknesses.[84] The frequency, intensity, and width of the peaks of in-plane E^1_{2g} and out-of plane A_{1g} vibrations were found to be strongly dependent on the number of layers. With decreasing numbers of MoS_2 layers, the E_{1g} mode shows a red-shift of 2 cm^{-1}, while the A1g mode is blue-shifted by 4 cm^{-1} (Fig. 5D), which is attributed to Columbic interactions and possible stacking-induced changes in the intra-layer bonding. The line width of the A_{1g} mode achieved a peak value for the two-layered MoS_2 nanosheets, whereas that of the E_{2g} mode does not depend on the thickness. Meanwhile, a large frequency shift of the shear mode to higher wave numbers was found in MoS_2 flakes with high numbers of layers.

4. Applications

4.1 Energy conversion from electrocatalysis

The progress achieved in MoS_2 electrocatalysts for HER provides a great opportunity for ameliorating the energy crisis. In this work, fundamental mechanistic studies on the molecular systems, supported by theory and DFT calculations, led to the identification of MoS_2 as a potential substitute for noble metal catalysts (Pt/C). Theoretical studies have identified the edges of MoS_2 as active sites for HER electro-catalysis, and these results were further confirmed by combination of the layered structure

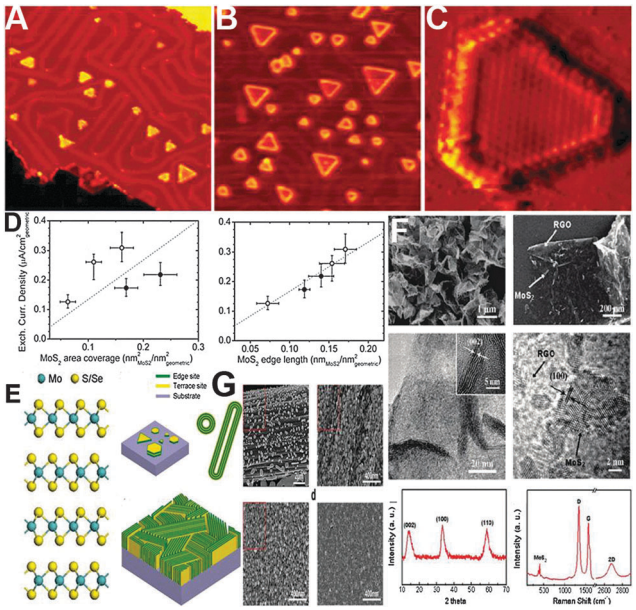

Fig. 6 (A–C) A series of STM images of MoS_2 nanoparticles on Au (111): (A) low coverage (0.06 nm^2 MoS_2 per nm^2 geom.), annealed at 400 °C (470 Å by 470 Å, 1.2 nA, 4 mV). (B) High coverage (0.23 nm^2 MoS_2 per nm^2 geom.), annealed to 550 °C (470 Å by 470 Å, 1.2 nA, 1.9 V). (C) Atomically resolved MoS_2 particle, from a sample annealed to 550 °C, showing the predominance of the sulfided Mo-edge. (D) Exchange current density *versus* (left) MoS_2 area coverage and (right) MoS_2 edge length. Copyright 2007, the American Association for the Advancement of Science. (E) Layered crystal structure of molybdenum chalcogenide with individual S–Mo–S layers stacked along the *c*-axis by weak van der Waals interaction. Copyright 2013, American Chemical Society. (F) MoS_2 nanoparticles on graphene in the MoS_2/RGO hybrid. Copyright 2011, American Chemical Society. (G) SEM images of the as-grown materials on the carbon fiber paper (CFP). Copyright 2013, American Chemical Society.

via a well-defined molecular model system. The atomic sites on edges of MoS_2 nanosheets have unsaturated coordination and dangling bonds, which play important roles in HER. By reducing the dimension along the in-plane direction, the edges of 2D MoS_2 are extensively exposed and the electronic and catalytic properties are effectively enhanced (Fig. 6A–D). In addition, these edge sites of MoS_2 have been demonstrated to possess metallic electronic states.[85] Importantly, the edge sites of MoS_2 have been demonstrated to be active catalytic centers for HER, in sharp contrast to HER-inert terrace sites.[21] Therefore, in order to design MoS_2 with the superior HER activity, it is important to expose large numbers of these catalytic points, which are especially prevalent in 2D MoS_2 nanosheets, indicating the potential for favorable HER performance with these 2D structures. However, due to its highly anisotropic character, the original 2D structure naturally converts to 3D along specific directions of the structure with formation of various morphologies, such as nanoplates,[86,87] nanoribbons,[61] or nanoparticles.[62]

4.1.1 Tuning the active sites. To preserve these active sites as much as possible, Cui's group synthesized MoS_2 films with vertically aligned layers.[15] The structure predominantly exposes the edges of the layers, exposing the edges on the film surface maximally (Fig. 6E). TEM images show the presence of densely packed, stripe-like grains, which indicates that the layers are all vertically aligned on the substrate. The edge-terminated surface is considered to be thermodynamically unstable due to the large surface energy of the edges, while a metastable morphology is likely to be obtained by kinetically overcoming the free energy barrier through rapid sulfurization.[88] Furthermore, reducing the size of the bulk MoS_2 material into nanostructured particles is another effective pathway toward maximizing exposure of active edge sites. Nanostructured MoS_2 with large surface curvature induces a high surface energy to enhance the number of exposed edges. Dai's group developed a selective solvothermal synthesis of MoS_2 nanoparticles on reduced graphene oxide (RGO) sheets (Fig. 6F). According to the X-ray diffraction (XRD) pattern, the broad diffraction peaks indicated that nanosized MoS_2 crystal domains with hexagonal structure were anchored on the RGO nanosheets. Furthermore, with RGO severing as a frame, the nanostructured MoS_2 was maintained with an abundance of exposed edges. Similarly, MoS_2 nanoparticles anchored on a 3D carbon fiber paper (CFP) substrate were successfully synthesized through pyrolysis and sulfurization methods. As shown in Fig. 6G, smaller nanoparticles bonded to the surface of the CFP, and the large surface curvature helps to expose more active sites and enhances the activity of the catalytic centers.

Additionally, some effective synthetic strategies have been utilized to extend the active edge sites in order to increase catalytic activity.[89–91] As observed in Fig. 7A, a facile method was applied for the synthesis of large-area contiguous thin films of an ordered mesoporous architecture of MoS_2 with a tunable film thickness exhibiting excellent catalytic activity for HER. By controlling the morphology, the surface structure of the catalyst was engineered at the atomic scale, enabling the active sites MoS_2 to be extensively exposed. Moreover, chemical exfoliation was an alternative effective pathway for MoS_2 with a large number of active sites.[19,92] Interestingly, simultaneous conversion of the 2H to 1T polymorph was achieved during the process, which increased the electric conductivity of the layered MoS_2. Chhowalla's group applied chemical exfoliation of intercalated MoS_2 prepared using butyllithium, for the preparation of MoS_2 with different crystal phases, and some deep insights into the mechanisms responsible for HER were provided (Fig. 7B).[93] MoS_2 nanosheets with high concentration of metallic 1T phases exhibited superior HER electrocatalytic performance, whose formation was catalyzed by Li^+ during the synthesis process.[94] To identify active sites in 2D mixed-phase MoS_2 sheets, the active edges in 2H or 1T MoS_2 nanosheets were chemically oxidized. The electrochemical oxidation led to a reduction in the HER for the 2H nanosheets, while unaffected catalytic performance was observed in chemical oxidation of the 1T phase, implying that the basal plane was catalytically active for HER performance. Furthermore, the catalytic activity of the 2H phase could be improved by increasing its conductivity through doping with metallic SWNTs, suggesting that charge transfer kinetics in metallic MoS_2 was another key parameter for achieving superior HER performance.

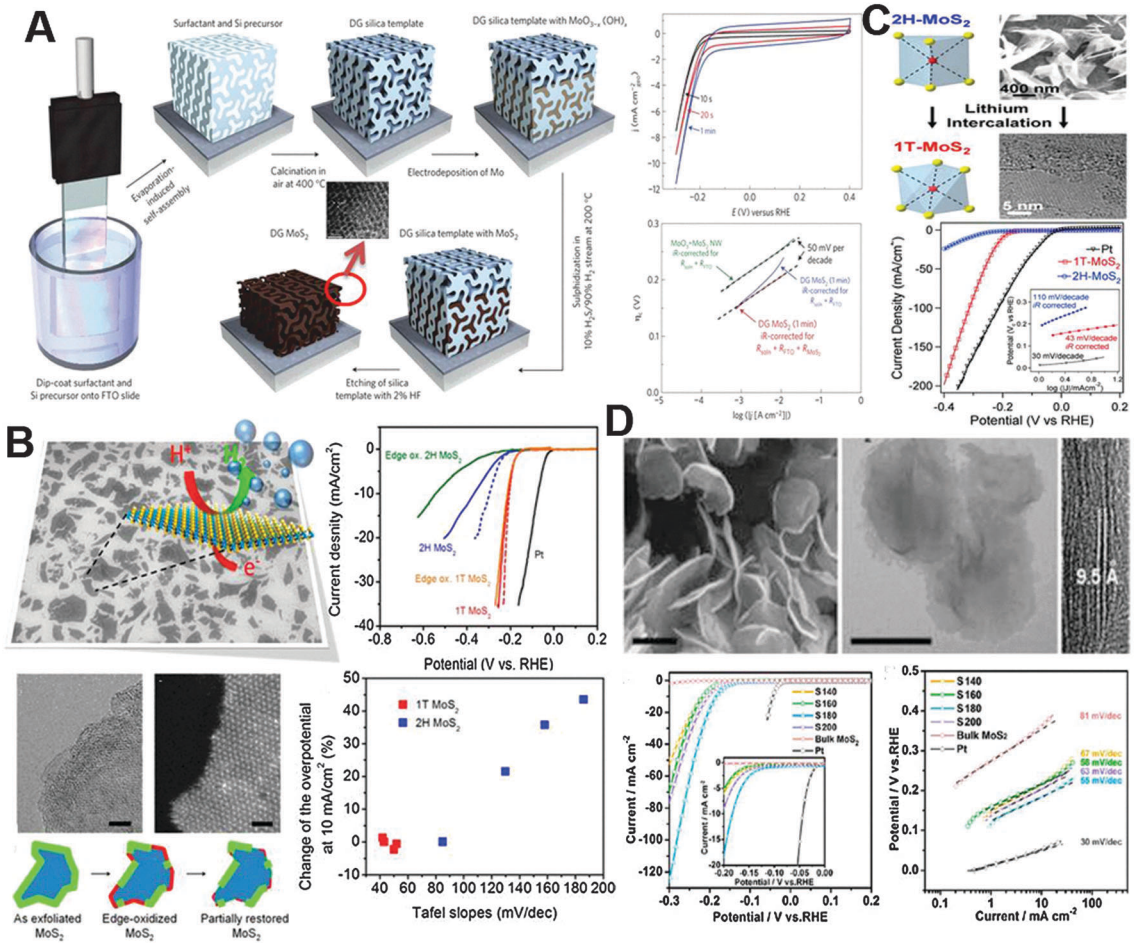

Fig. 7 (A) The synthesis procedure and structural model for mesoporous MoS_2 with a double-gyroid (DG) morphology with the TEM images of the double-gyroid MoS_2 inset, and the HER performance. Copyright 2012, Macmillan Publishers. (B) Electron microscopy images of chemically exfoliated MoS_2 and the HER activity of the exfoliated MoS_2 nanosheets. High-resolution TEM and HAADF STEM of the edge-oxidized MoS_2 nanosheets showing corrugated edges caused by chemical oxidization. Schematic of the oxidation process and partial restoration of nanosheet edges after several voltammetric cycles. The variation of overpotential at 10 mA cm^{-2} and Tafel slopes for 1T and 2H MoS_2 for the samples and after the 1st, 2nd, and 150th voltammetric cycles. Copyright 2013, American Chemical Society. (C) The electrocatalytic performance of chemically exfoliated and as-grown MoS_2 nanosheets. Polarization curves at higher and lower potentials with corresponding Tafel plots (inset). Copyright 2011, American Chemical Society. (D) FESEM image, TEM image and cross-sectional TEM images of the MoS_2 nanosheets synthesized at 180 °C, and polarization curves and Tafel plots of the oxygen-incorporated MoS_2 nanosheets. Inset: Enlargement of the region near the onset. Copyright 2013, American Chemical Society.

In addition to chemical exfoliation, CVD methods have been applied to prepare the mixed-phase MoS_2. As shown in Fig. 7C, low overpotentials (187 mV) requiring an electrocatalytic current density of 10 mA cm^{-2} and a reduced Tafel slope (43 mV $decade^{-1}$) were observed in the HER process. According to structural characterization along with electrochemical studies, it is reasonable to speculate that MoS_2 with the 1T phase exhibited some superior characteristics for boosting electrocatalytic HER performance, such as facile electrode kinetics, low-loss electrical transport, and an increased density of active sites for catalysis.[95] Hence, the distinct features of the 1T phase endowed the MoS_2 with highly competitive properties compared to existing HER catalysts. Therefore, in order to increase HER performance, simultaneous optimization of both active sites and electronic conductivity for MoS_2 electrocatalysts should be the most effective path. However, due to the contradictory relationship between active sites and conductivity, this situation cannot be easily achieved. As mentioned above, abundant active sites are prone to appear in these small MoS_2 nanostructures with large numbers of active sites, but the conductivity in such structures is hindered due to the poor electron transport. Recently, Xie's group reported a facile hydrothermal method to fabricate defect-rich MoS_2 nanosheets with exposure of active edges.[68] According to theoretical simulation, the formation of the nanodomains with quasi-periodic arrangement along MoS_2 nanosheets greatly promotes the conductivity of MoS_2, providing an opportunity for the coordination of the high conductivity with a high number of active sites for MoS_2 catalysts. According to theoretical calculations, the degree of disorder in oxygen-incorporated MoS_2 ultrathin nanosheets can be regulated to obtain the balance between the active sites and conductivity, thereby providing synergistic structure and electronic modulations for high HER performance (Fig. 7D).[96,97] In order to prove the incorporation of oxygen atoms into MoS_2, the atomic

ratio of Mo : S in the samples was determined through compositional analysis and found to vary from 1 : 2.02 to 1 : 2.10; this confirmed that the degree of disorder was dependent on the unsaturated sulfur atoms. Moreover, according to the results of EIS, the high concentration of effective active sites and high conductivity in the nano-sheet determined the HER activity. In the oxygen incorporated MoS_2 nanosheets, a large cathodic current density of 126.5 mA cm^{-2} at 300 mV with the Tafel slope of 55 mV $decade^{-1}$ was achieved.

4.1.2 Composite materials. As is well known, conductivity plays the key role in the performance of high-activity electrocatalysts. The poor conductivity of MoS_2 can be ameliorated by the preparation of composites containing conductive additives.[98–101] Tsai and his coworkers have applied DFT to predict the support effects for MoS_2 with different catalyst supports on the hydrogen adsorption free energy at the MoS_2 Mo-edge and S-edge sites. They concluded that a general trend for the Mo-edge sites could be seen, and that stronger adhesion of the MoS_2 catalyst onto the support led to weaker hydrogen binding. The results suggested that the support was crucial for determining the HER activity of supported MoS_2 and the catalytic activity at the Mo-edge could be optimally tuned (Fig. 8A). Furthermore, the direct anchoring of MoS_2 to a support with robust conductivity ensured a low resistance electrical transport pathway as well as reduced physical delamination, which enhanced its stability. Au foil was applied as the conductive support for preparation of MoS_2 nanosheets through a LPCVD route.[64] The MoS_2 composite, synthesized at low growth temperature with high crystal quality, monolayer thickness, tunable size, and transferability to other substrates, has the potential for applications in high HER performance electrocatalysis. A rather low Tafel slope (61 mV $decade^{-1}$) and a relatively high exchange current density of 38.1 μA cm^{-2} were achieved (Fig. 8B). The superior HER performance was derived from electron coupling between MoS_2 and Au foils. Similar support effects have been clearly demonstrated for MoS_2 nanoparticles synthesized on RGO, as observed in Fig. 8C, the obtained catalyst exhibited enhanced intrinsic electrocatalytic performance toward HER compared to unsupported MoS_2 particles.

The MoS_2 nanoparticles on RGO sheets were obtained *via* a facile solvothermal approach. With its high density of exposed edges and excellent electrical coupling to the underlying conductive graphene, the MoS_2/RGO hybrid material exhibited excellent HER activity with a small overpotential of ~100 mV, large cathodic currents, and a Tafel slope as small as 41 mV $decade^{-1}$. Thus, the approach of carrying out materials synthesis on RGO has led to an advanced MoS_2 electrocatalyst with highly HER performance. Similarly, carbon nanotubes (CNTs) were also utilized as the conductive support, and a MoS_2/NCNT forest catalyst was fabricated *via* a low-temperature precursor decomposition method.[102] As depicted in Fig. 8D, the hybrid catalyst had a morphology consisting of an electro-conductive N-doped CNT forest densely coated with ~2 nm scale amorphous MoS_2 catalysts. In the hybrid structure, the protonated N showed greatly improved surface energy and can not only provide favorable reaction affinity toward MoS_2 precursors, avoiding the need for an adhesive layer, but also provide additional electrons to the graphitic carbon to maintain high conductivity.[103] The catalyst exhibited outstanding HER catalytic activity with an overpotential of 75 mV. In addition, only a minor deterioration of the current was observed after 1000 cycles. As for practical applications, the fabrication of MoS_2 on CFP was also reported *via* a pyrolytic synthesis using MoO_3 NPs.[104] MoS_2 NPs with a diameter of 30 nm were obtained by a rapid sulfurization process, the scheme of which is depicted in Fig. 8E. To further enhance the HER performance of as-grown 2H MoS_2, the catalyst was treated electrochemically with Li for layer exfoliation and 1T phase formation. Therefore, this system combined a high concentration of exposed edges, protected by the CFP, and the 1T phase, generated by Li electrochemical treatment. The achievement of 200 mA cm^{-2} current at 200 mV overpotential and long-term stability promise high potential for practical applications.

Besides the application of supports with high conductivity, the utilization of materials with electrocatalytic HER activity as substrates is an effective alternative method. Yu's group anchored MoS_2 onto the $CoSe_2$ nanobelts by using a solvothermal process (Fig. 9A).[70] As observed in the HRTEM images in Fig. 9B, layered MoS_2 nanosheets, with an interlayer separation of 0.63 nm, were grown on $CoSe_2$. The anchoring of MoS_2 on $CoSe_2$ generated more active edge sites. Meanwhile, $CoSe_2$ chemically interacts with MoS_2 by the formation of S–Co bonds, which can further improve the HER activity of MoS_2. This is because Co, as a first-row transition metal ion, can promote the HER activity of MoS_2 by coupling with the S-edges to lower ΔG_H from 0.18 to 0.10 eV to afford faster proton adsorption kinetics.[105,106] Therefore, in this hybrid catalyst, the $CoSe_2$ nanobelts can not only couple with MoS_2 to promote the HER activity, but also serve as an effective substrate for mediating the growth of MoS_2 to form more active HER sites. The MoS_2/$CoSe_2$ catalyst showed exceptional HER catalytic properties in an acidic electrolyte with an onset potential of a mere −11 mV, a small Tafel slope of 36 mV $decade^{-1}$ and high exchange current density (Fig. 9C).

In addition, Jaramillo's group reported the introduction of sulfur atoms into the surface of molybdenum phosphide (MoP) by a post-sulfidization treatment of MoP in a H_2S atmosphere, to produce a molybdenum phosphosulfide (MoP/S).[107] The composite catalyst exhibited high HER performance and remained stable in accelerated durability testing. The superior performance might be derived from synergistic effects between sulfur and phosphorus atoms, and this process produced a high-surface-area electrode that was more active than those based on the pure sulfide or the pure phosphide. Moreover, the fabrication of amorphous MoS_xCl_y was reported *via* a LPCVD method, and found to be a high-performance electrocatalyst for electrocatalytic hydrogen generation.[108] MoS_xCl_y exhibited stable and high catalytic activity toward HER, which was evidenced by the large current densities at low overpotentials and the low Tafel slopes. It was clearly found that the addition of a Cl atom in MoS_2 modified the electronic structure of the catalyst, which was due to the substitution of Cl into the ternary

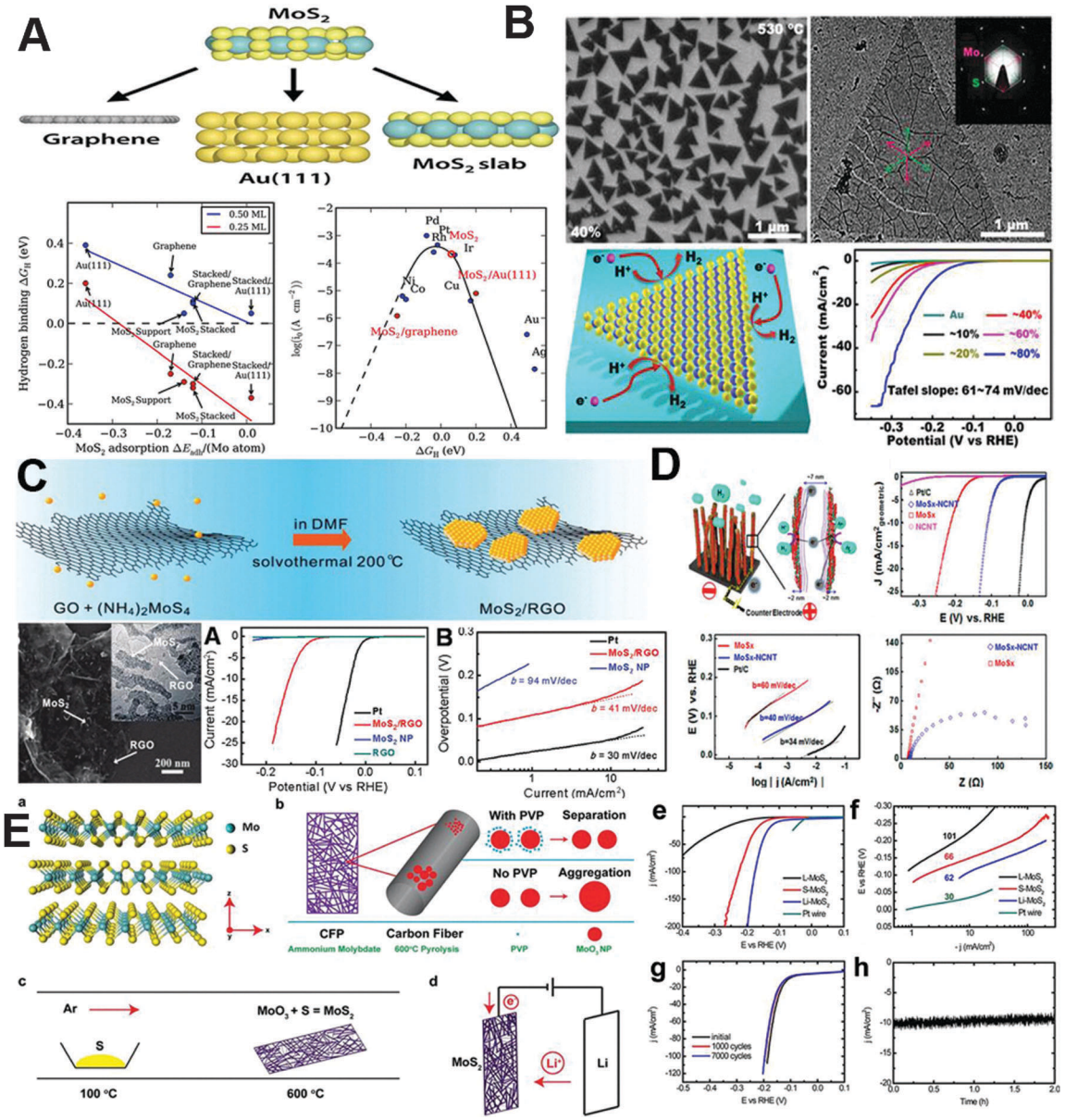

Fig. 8 (A) Change in hydrogen adsorption free energy on the Mo-edge at each coverage with MoS_2 adsorption onto the support. The activity maps for HER showed the exchange current density as a function of the calculated free energy of hydrogen adsorption. Copyright 2014, American Chemical Society. (B) SEM and TEM images of MoS_2 flakes with different coverages on Au foil. The polarization curves and the corresponding Tafel plots indicated the coverage-dependent HER activity of as-grown monolayer MoS_2 on Au foils. Copyright 2014, American Chemical Society. (C) Schematic solvothermal synthesis with GO sheets to afford the MoS_2/RGO hybrid, and the SEM and TEM images of the MoS_2/RGO hybrid. The polarization curves of the as-indicated catalysts and Tafel plots recorded on glassy carbon electrodes with a catalyst loading of 0.28 mg cm^{-2}. Copyright 2011, American Chemical Society. (D) Scheme for the MoS_x/NCNT forest hybrid catalyst, and the polarization curves and Tafel plots of different catalysts. EIS for the MoS_x/NCNT and bare MoS_x at −0.2 V *versus* RHE from 5 MHz to 10 mHz. Copyright 2014, American Chemical Society. (E) (a) Schematic of the synthesis of large and small MoO_3 NPs on CFP. (b) The CFP was first dipped into the ammonium molybdate solution with or without the PVP additive. (c) During the pyrolysis at 600 °C, the surface of the nucleated NPs may be coated by PVP molecules, which prevents those particles from further aggregation. Without the addition of PVP, the small particles tend to aggregate during the process and form large particles in the end. (d) Schematic of the rapid sulfurization setup in a horizontal tube furnace. (e–h) Electrochemical characterization of as-grown catalysts on CFP. 2014, American Chemical Society.

MoS_xCl_y and the introduction of defect states within the band gap. Therefore, the changed structure decreased the Gibbs free energy for hydrogen adsorption on the catalyst.

4.1.3 Perspective. In summary, various approaches have been applied to achieve high-performance in HER, *e.g.*, increasing the number of active sites, modification of the phase structure, and doping or substitution in MoS_2. Still, there is much considerable room for improvement in the development of MoS_2 with higher HER performance. For example, band structure and Fermi level tuning may become powerful tools; in this case, we should balance a combination of theoretical, fundamental, and performance-based studies to address our growing energy

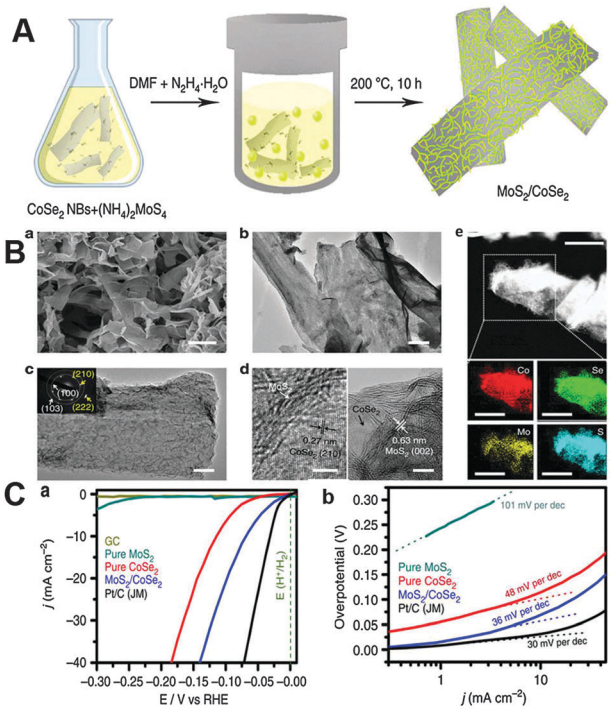

Fig. 9 (A) Schematic illustration of the preparation of a $MoS_2/CoSe_2$ hybrid. (B) Scanning electron microscopy image of the $MoS_2/CoSe_2$ hybrid (a). Scale bar, 800 nm. (b and c) TEM images with different magnifications of the $MoS_2/CoSe_2$ hybrid. Scale bars, 200 and 50 nm, respectively. The inset in c shows the corresponding SAED pattern. (d) HRTEM images of the $MoS_2/CoSe_2$ hybrid showing distinguishable microstructures of MoS_2 and $CoSe_2$. Scale bars, 5 nm. (e) STEM-EDX elemental mapping of the $MoS_2/CoSe_2$ hybrid showing clearly the homogeneous distribution of Co (red), Se (green), Mo (yellow) and S (azure). Scale bars, 200 nm. (C) Polarization curves for HER on the bare GC electrode and modified GC electrodes comprising the $MoS_2/CoSe_2$ hybrid, pure MoS_2, pure $CoSe_2$ and a high-quality commercial Pt/C catalyst. Catalyst loading is about 0.28 mg cm^{-2} for all samples (a). Sweep rate: 2 mV s^{-1}. (b) Tafel plot for the various catalysts derived from (a). Copyright 2015, Macmillan Publishers.

demand. In the field of practical applications, the synthesis of large-scale and high quality MoS_2 needs to be further promoted.

4.2 Applications in photoelectrochemical systems

Solar light, as a clean and cost-free resource, can be utilized in the pursuit of renewable energy. Solar-driven water splitting, one of the most promising approaches for preparation of H_2, can be achieved by photoelectrochemical (PEC) systems. Due to the fast recombination of the electron–hole pairs, the majority of photocatalysts cannot provide a high efficiency in the hydrogen evolution even in the presence of sacrificial agents. In order to retard recombination of the photogenerated charge carriers, the noble metals as co-catalysts have been commonly applied to achieve high performance in previous studies. The use of co-catalysts not only effectively separated the electron–hole pairs but also provided active sites for the reactions. Accordingly, the application of the low-cost noble-metal free co-catalysts with high efficiency is of great value for practical development of hydrogen technology.

Recently, Kanda *et al.* coupled MoS_2 with TiO_2, and the as-prepared photocatalyst exhibited good activity toward hydrogen generation under UV light irradiation.[109] In contrast to pure TiO_2, the loading of 0.043% of MoS_2 onto the surface of TiO_2 increased the rate of H_2 generation by two orders of magnitude. Importantly, the matched electronic structure guaranteed the photostability of MoS_2. The improved performance might be attributed to the high electrocatalytic activity of MoS_2 for the reduction of water. In addition, Li and his co-workers reported the enhancement of photocatalytic H_2 evolution on CdS/MoS_2 by using a lactic acid solution as a sacrificial agent under visible-light irradiation.[110] As co-catalysts, the loading of MoS_2 on CdS led to a higher photoactivity than the noble metals, which was attributed to the formation of a phase junction between CdS and MoS_2 that could greatly enhance photocatalytic activity for H_2 production. However, the poor electrical conductivity of MoS_2 restricts its cocatalytic activity, which can be ameliorated by tuning the phase structure or forming a composite with other conducting materials. Kun *et al.* reported the fabrication of a nanosized layer-structured MoS_2/graphene nanosheet loaded with CdS nanoparticles by a wet chemistry synthetic method (Fig. 10A and B) and investigated the H_2 production activity under visible light. The catalyst not only could reduce the recombination probability of photo-excited charge carriers but also could provide abundant reactive sites for hydrogen evolution. After loading graphene with MoS_2, the composite exhibited an enhanced photocatalytic activity for HER with about 9 mmol evolved in 5 h from a 0.5 wt% mixture, almost 1.5 times higher than that obtained with MoS_2/CdS (Fig. 10C). Furthermore, after several cycles, the hydrogen generation rate of MoS_2/G–CdS almost remained constant at 1.8 mmol h^{-1}, indicating its stability. Serving as the 2D layered conductor in the composite, graphene matched well with layered MoS_2 and enhanced its conductivity, facilitating fast charge transfer. The photogenerated electrons derived from CdS transferred to the edges of MoS_2 through the conducting sheets and then reacted with the H^+ to form H_2.

Notably, the relationship between the light absorber that generates electron–hole pairs and the electrocatalyst that facilitates charge transfer determines the overpotential for H2 production. Ding *et al.* integrated a heterostructure of exfoliated 1T-MoS_2 and planar p-Si as a photocathode for the PEC hydrogen generation (Fig. 10D).[111] Under simulated 1 sun irradiation illumination, a current density of 17.6 mA cm^{-2} at 0 V *vs.* the reversible hydrogen electrode (RHE) and an excellent onset of photocurrent are achieved with good stability (Fig. 10G). In comparison with the semiconducting 2H-MoS_2 phase, electrochemical impedance spectroscopy (EIS) confirmed the smaller charge transfer resistance from Si to MoS_2, enhancing the electrode kinetics of 1T-MoS_2/Si for HER. Additionally, the results of surface photoresponse (SPR) measurements showed that fast and irreversible electron transfer took place from Si to 1T-MoS_2, inhibiting the recombination of the photogenerated charge carriers. This also contributed to the superior performance of

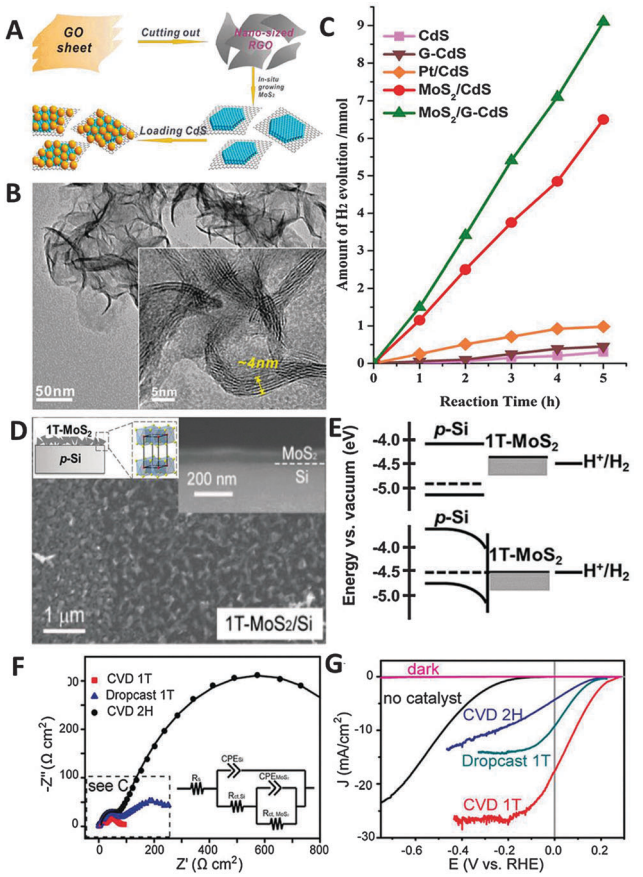

Fig. 10 (A) Schematic illustration of the growth mechanism of MoS_2/G–CdS composites. (B) TEM image of the MoS_2/G composite after annealing at 573 K for 2 h in an Ar atmosphere in which the molar ratio of MoS_2 to graphene is 1 : 2. (C) The amount of H_2 photocatalyzed by CdS, MoS_2/CdS, MoS_2/G–CdS, graphene/CdS, and Pt/CdS within 5 h. Copyright 2014, American Chemical Society. (D) SEM images of 1T-MoS_2/Si fabricated by the CVD method. (E) Schematic band energy diagram of p-Si, 1T-MoS_2, and H^+/H_2 redox couple at 0 V *vs.* RHE in the dark before and after equilibrium. (F) Nyquist impedance plots and (G) the *J*–*E* curves of a CVD-grown 2H-MoS_2/Si photocathode (CVD 2H), a CVD grown 1T-MoS_2/Si photocathode (CVD 1T), and a dropcast 1T-MoS_2/Si photocathode (dropcast 1T) measured in 0.5 M H_2SO_4 under simulated 1 Sun irradiation. Copyright 2014, American Chemical Society.

these 1T-MoS_2/Si photocathodes. However, the oxidation of Si to form SiO_2 caused problems with this approach; in order to resolve this issue, Chorkendorff and his co-workers deposited a thin layer of Ti on Si. The Ti layer not only acted as a conductive protection layer, but also enhanced the stability by the formation of TiO_x. In addition, the enhanced conductivity from this thin tunnel barrier contributed to its high HER performance, which was noticeably better than that of a pure Si electrode. The MoS_2–Ti–Si electrode exhibited comparable activity to that of the Pt electrode. Because of the protection afforded by the Ti layer, the electrode maintained an unprecedented anodic onset for the HER for a non-Pt catalyst in acidic medium even after 1 h.

Heterostructures of MoS_2 on p-type semiconductors exhibit high activity and stability, and are the promising alternatives to noble metal catalyst-based photocathodes. Accordingly, the development and practical application of MoS_2-based PEC solar energy conversion are of great urgency for the utilization of clean solar energy.

4.3 Energy conversion from mechanical stress

Piezoelectricity can arise in crystal structures with the broken inversion symmetry, allowing robust conversion between electrical and mechanical force.[112,113] With their ability to withstand enormous strain,[114] two-dimensional materials are of great interest as high-performance piezoelectric materials. Due to the lattice distortion induced by strain and the associated charge polarization, monolayer MoS_2 is theoretically predicted to be strongly piezoelectric, an effect that disappears in the bulk counterparts because of the opposite orientations between adjacent layers.[115] Stretching and releasing of odd-layer MoS_2 causes an oscillating electrical charge, providing an ideal platform for converting mechanical energy into electricity.

On this basis, Wang and his coworkers developed a MoS_2-based nanogenerator. The layers of MoS_2 were exfoliated onto a polymer stack consisting of water-soluble polyvinyl alcohol on a Si substrate. The few-layered MoS_2 flakes were identified first using an optical microscope and the thickness was then measured by atomic force microscopy and confirmed by Raman spectroscopy. In addition, the second-harmonic generation (SHG) was used to determine the crystallographic orientation of the layered MoS_2. A typical device with single-layer MoS_2 outlined by a dashed border is depicted in Fig. 11A. After mechanically bending the substrate, strain (limited to 0.8%) was applied to the MoS_2 flakes proportional to the bending radius. The piezoelectric response was studied by applying strain to a device coupled with an external resistor. The induced charges at the MoS_2 edges can drive the flow of electrons in the circuit. With the release of strain, the electrons flowed back. Current outputs were observed after variation of external strain in the *x* direction, demonstrating the conversion of mechanical energy into electricity. A positive output was observed with increasing strain, while a negative output was shown after releasing the strain (Fig. 11B). The responses were proportional to the magnitude of the applied strain: for 1% change in strain, the peak open-circuit voltage and current of 18 mV and 27 pA increased to 32.8 mV and 55.1 pA. Furthermore, the evolution of the signal was investigated with increasing numbers of layers (*n*). MoS_2 with even layers is expected to be centro-symmetric and thus lose both its piezoresponse and SHG signal. In contrast, in samples with the odd number of layers, the piezoresponse and SHG are retained. As shown in Fig. 11C, the SHG intensity was strong for n = 1, 3, 5 and disappeared for n = 2, 4, 6 and bulk. Almost no detectable current output can be seen for even-layer samples. For odd-layer samples the piezoelectric output is large, although it decreases as the layer number increases. In order to boost the piezoelectric output, four pieces of single-layer MoS_2 flakes were carefully integrated. By connecting these 2D MoS_2 flakes in series, enhancements in output voltages or currents were observed. This suggests the possibility of practically achieving energy conversion from the piezoelectric output by using large-scale 2D piezoelectric nanomaterials. Additionally, the robust

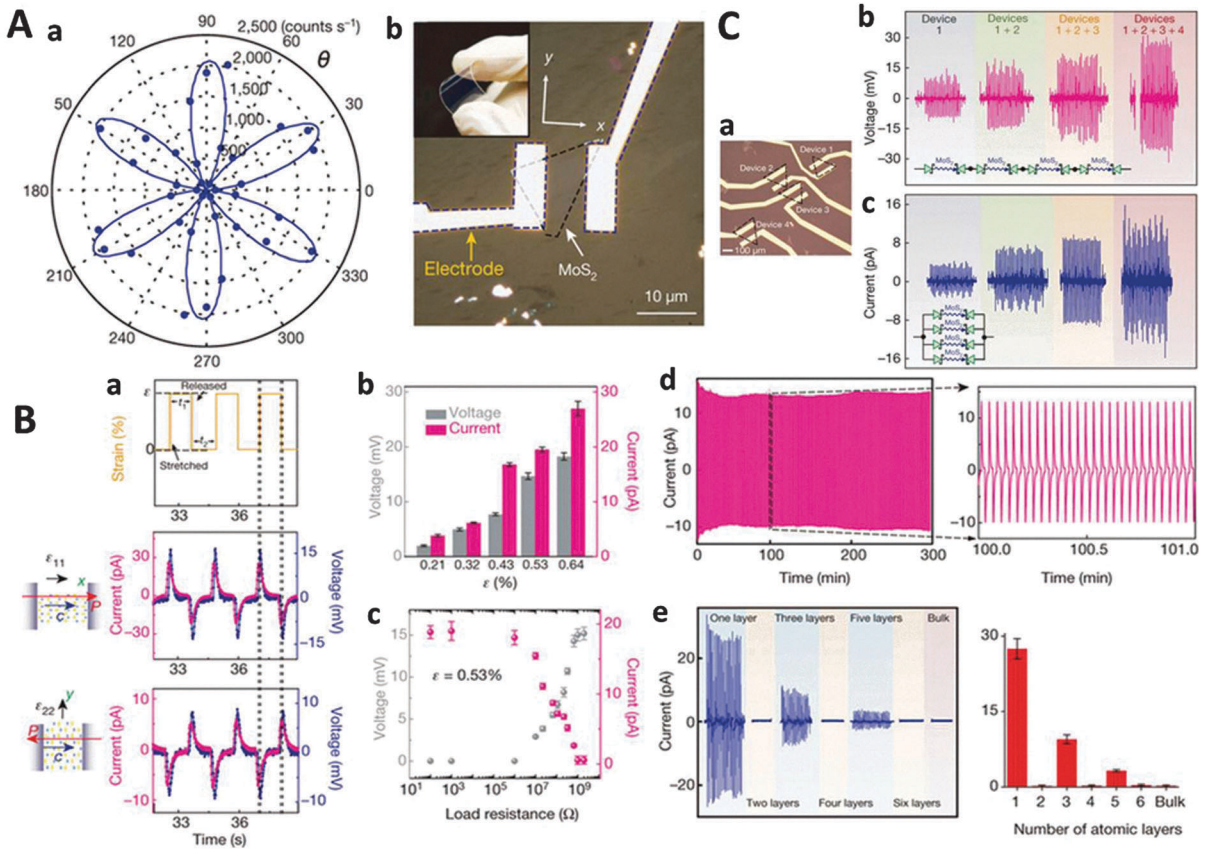

Fig. 11 (A) (a) Polar plot of the SH intensity from single-layer MoS_2 as a function of the crystal's azimuthal angle θ. The symbols are experimental data and the solid lines are fits to the symmetry analysis described in the text. (b) A typical flexible device with single-layer MoS_2 flakes and electrodes at its zigzag edges. Inset: Optical image of the flexible device. (B) Voltage response with 1 GV external load and short-circuit current response of a single-layer MoS_2 device under periodic strain in two different principal directions. Top: Applied strain as a function of time. Middle: Piezoelectric outputs from single-atomic-layer MoS_2 when strain is applied in the *x* direction (armchair direction). Bottom: Corresponding piezoelectric outputs from the same device when strain is applied in the *y* direction (zigzag direction). The phase difference highlighted by black dashed lines is obtained by theoretical derivation and has been intentionally exaggerated for clarity, not experimental measurement. Red, blue and black arrows represent the directions of polarization, the polar axis of MoS_2 and principal strains, respectively. (b) Dependence of piezoelectric outputs from a single-layer MoS_2 device on the magnitude of the applied strain. Mean values from 20 technical replicates are indicated. Error bars represent s.d. (c) Dependence of voltage and current outputs from a single-layer MoS_2 device under 0.53% strain as a function of load resistance. Mean values from 20 technical replicates are indicated. Error bars represent s.d. (d) Cyclic test showing the stability of the single-layer MoS_2 device for a prolonged period. (e) Evolution of the piezoelectric outputs with increasing number of atomic layers (n) in MoS_2 flakes. For each device, mean values from 20 technical replicates are indicated. Error bars represent s.d. (C) Array integration of CVD single-layer MoS_2 flakes. (a) Optical image of an array consisting of four CVD single-layer MoS_2 flakes. (b) Constructive voltage outputs by serial connection of the individual flakes in the circuit. (c) Constructive current outputs by parallel connection of the individual flakes in the circuit. Copyright 2014, Macmillan Publishers.

piezoelectricity of two dimensional MoS_2 materials makes them excellent material choices for the fabrication of nanoscale electromechanical systems, ultrasensitive sensors and generation of electricity for low-power electronics.

4.4 Applications in energy storage devices

Efficient energy storage is a long-standing technological and scientific problem that has global implications for humanity.[116,117] Due to the low atomic weight and the high absolute potential value of Li, the Li-ion battery (LIB) has been considered as a highly efficient energy storage system, with theoretical energy density values up to 400 W h kg^{-1}.[118] As for the development of advanced lithium ion batteries with smaller scale and larger capacity, the selection of suitable materials is still a promising field of research. Due to their typical layered structure, Li^+ ions can easily intercalate between the layers of MoS_2. The highest reported specific capacity for MoS_2 was 1131 mA h g^{-1} with a current of 50 mA g^{-1}. It was found that the charge capacity of bulk MoS_2 tended to sharply decrease after cycling, whereas the nanosheets prepared from chemical lithiation and exfoliation exhibited stability and retained a high capacity of 750 mA h g^{-1} even after 50 cycles.[119] However, the capacity fading and inferior high rate properties of the MoS_2 anode are the main obstacles for the final applications. A large number of research groups have focused their attention in promoting the electrochemical performance of the MoS_2-based anodes by fabricating MoS_2–carbon composites or broadening the interlayer distance. According to the results of the increased

charge capacity value (up to 1290 mA h g^{-1}) in MoS_2–graphene composites,[29] the higher capacity, excellent rate capability, and long cycle life were further realized in the MoS_2NS–RGO composite.[120] Moreover, Chen and his coworkers fabricated the MoS_2/graphene composite by using the L-cysteine assisted solution-phase method. The composite with a Mo/C molar ratio of 1 : 2 exhibited the capacity of ~1100 mA h g^{-1} at a current of 100 mA g^{-1}, as well as excellent cycling retention and high rate performance.[121] Besides, the MoS_2@CMK-3 composite consisting of confined nanosized MoS_2 in the CMK-3 carbon matrix was recently reported.[120,122] The MoS_2@CMK-3 electrode was able to deliver a high discharge capacity of 934 mA h g^{-1} after 150 cycles at a current density of 400 mA g^{-1}. Also, the interplanar space (*d*-spacing) played a decisive role in lithium ion diffusion in the solid state phase of the MoS_2 anode. The MoS_2@TiO_2 hybrid structures showed the improved cyclic capacity retention and rate capability.[123] Liu *et al.* have developed a vacuum assisted impregnation route to prepare a highly ordered mesoporous MoS_2 with expanded *d*-spacing of the (002) plane (0.66 nm), providing sufficient space for ultra-fast lithium ion intercalation.[124] Similarly, the spacing of the (002) crystal plane was significantly expanded in the hierarchical MoS_2 nanoflake array/carbon cloth, thereby the high specific capacity, good cycling stability, and the predominant rate performance were achieved.[125]

Supercapacitors are also one of the most widely studied energy storage devices due to their high power density, high rate capability and long cycle life.[126] Based on their storage mechanism, supercapacitors are classified into two types: electrochemical double layer capacitors (EDLSs) and pseudocapacitors. The capacitance of EDLSs arises from electrostatic adsorption of ions at the interface between the electrode and electrolyte (non-Faradaic charge storage). Pseudocapacitors operate by a different mechanism, where reversible Faradaic processes take place and chemical reactions occur within active materials and electrolytes. Thorough investigations of the origin of pseudocapacitance have revealed that the ion intercalation plays a crucial role in energy storage, for example the intercalation of Li^+ into Nb_2O_5.[127] The weak van der Waals interaction between S–Mo–S layers allows easy intercalation of foreign ions (H^+, Li^+) in MoS_2. Furthermore, Mo atoms are able to adopt a range of oxidation states from 2+ to 6+, enabling potential for pseudo-capacitance behavior with high specific capacitance for MoS_2 nanosheets.[128]

A typical example of ion intercalation is the use of 1T phase MoS_2 nanosheets as electrode materials (Fig. 12A–G).[129] The metallic 1T phase MoS_2 was demonstrated to be an attractive electrode material for supercapacitors due to its intrinsic hydrophilicity and high conductivity combined with excellent pseudocapacitance *via* ion intercalation. In this study, 100% monolayered MoS_2 nanosheets were obtained through chemical exfoliation of bulk MoS_2. A 1T MoS_2 film could be fabricated by restacking the suspended nanosheets using a simple filtration technique without any additives. The restacked MoS_2 was able to electrochemically intercalate various ions (H^+, Li^+ Na^+ and K^+) with extraordinary efficiency and showed high volumetric capacitance ranging from 400 to 700 F cm^{-3}. In non-aqueous electrolytes, the 1T MoS_2 shows an energy density and power density as high as 0.11 W h cm^{-1} and 1.1 W cm^{-3}, respectively. Cyclic stability testing of 1T phase MoS_2 showed that the electrode retained a capacitance in excess of 90% over multiple cycles. The coulombic efficiency in various electrolytes at a current rate of 2 A g^{-1} was as high as 90–98%. Tour *et al.*[130] reported the fabrication of an edge-oriented MoS_2 thin-film by electrochemical anodization of molybdenum metal followed by sulfur vapor treatment (Fig. 12H–J). The cyclic voltammograms of the edge-oriented MoS_2 thin-film electrode indicated that the pseudocapacitance could be attributed to cation intercalation and reversible redox reactions between different valence states of Mo (4+ to 3+). The voltammograms retained quasi-rectangular shapes even at scan rates as high as 100 V s^{-1} in 1 M LiOH solution. Furthermore, the quasi-triangular shape of galvanostatic charge/discharge curves indicated combined EDLC and pseudocapacitance behavior. The areal capacitance (C_A) of this flexible all-solid-state supercapacitor device increased from 2.2 to 10.5 mF cm^{-2} after 10 000 testing cycles at a current density of 10 mA cm^{-2}. The increase in the C_A is probably due to the presence of more activated edges. This finding indicated that cation intercalation plays a major role rather than Mo redox reactions. Therefore, optimization of architectures would enable MoS_2 with enhanced surface area and more activated edges for ion intercalation, thereby superior performance of supercapacitors can be obtained. Another example worth noting is the work by Yang *et al.*,[131] who reported a 2D MoS_2-based micro-supercapacitor. This MoS_2 micro-supercapacitor was fabricated through laser patterning of a spray-coated MoS_2 film and consisted of finger-like electrodes built from curly MoS_2 nanosheets. The flexible micro-supercapacitor exhibited high C_A (8 mF cm^{-2}) and volumetric capacitance (178 F cm^{-3}) and good cyclic performance (8% loss of capacitance after 1000 cycles).

In addition, other factors such as morphology, structure and size have also been shown to be important parameters in the performance of supercapacitors. Wang *et al.*[132] reported 3D flower-like MoS_2 nanostructures obtained through a two-step hydrothermal treatment of MoO_3 nanorods. This pure MoS_2 showed a high specific capacitance of 168 F g^{-1} at 1 A g^{-1} in 1 M KCl solution. In addition, these MoS_2 materials showed excellent long-term cyclic stability. The capacitance still remained at 92.6% after 3000 cycles of charge–discharge at a current density of 1 A g^{-1}. Other morphologies such as flower-like microspheres,[133] spherically MoS_2 clusters,[134] and MoS_2 spheres[135] have also been reported.

However, the main drawback of this approach is that the conductivity of MoS_2 is too low for its effective implementation in electrodes. Although the synthesis of MoS_2 can be well controlled, the structures of the active materials might become untailored after the electrode fabrication process.[136] Hence, rational design of architectures based on forming hybrids with conducting materials is important to fully utilize MoS_2 in high-performance supercapacitor electrodes. Graphene is also a 2D material and has good electrical conductivity with a large theoretical specific

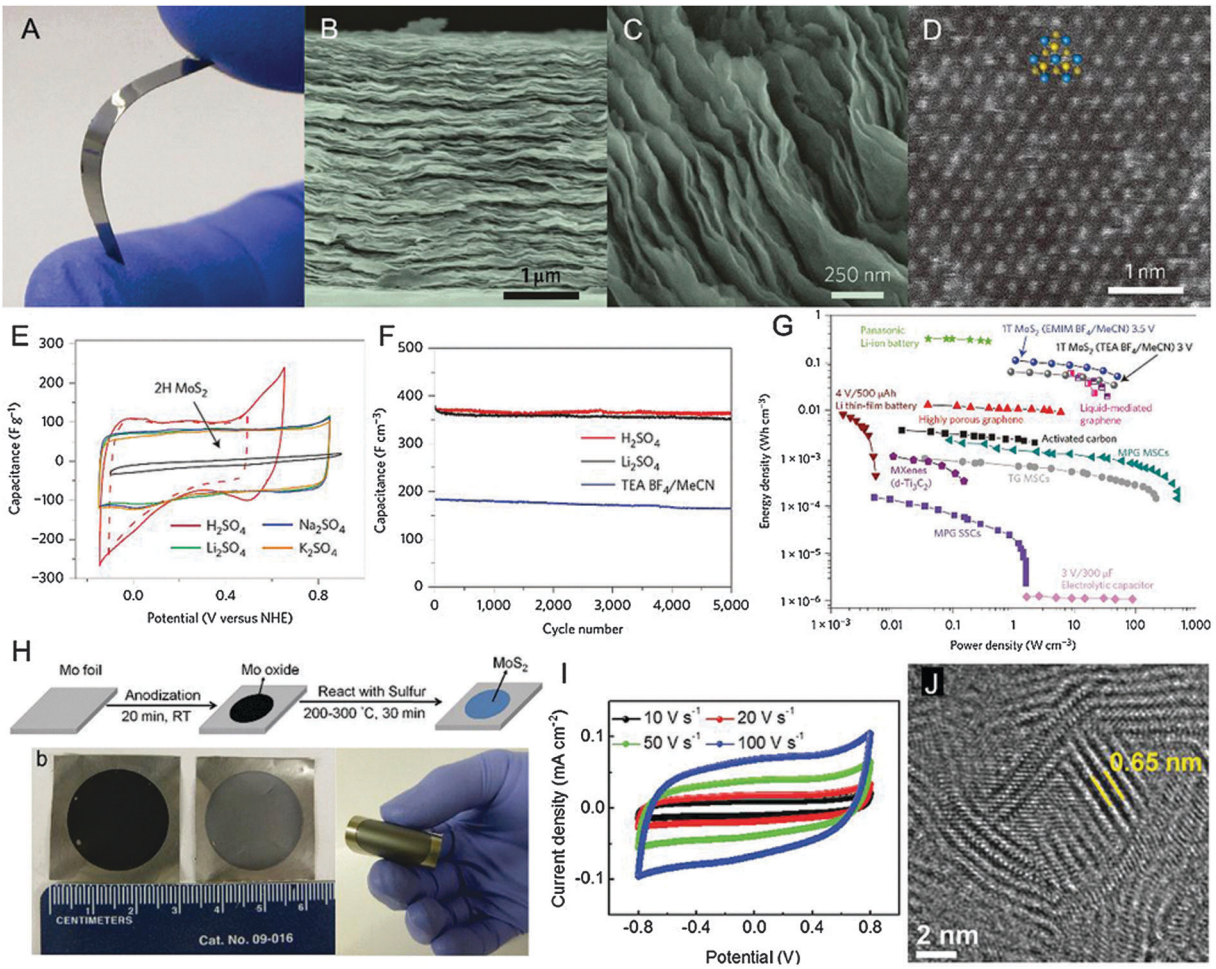

Fig. 12 (A) Photograph of chemically exfoliated 1T MoS_2 film on a flexible polyimide substrate (B) SEM image of the electrode showing the layered nature of the film made by restacking exfoliated 1T MoS_2 nanosheets. (C) High-magnification image of restacked MoS_2 nanosheets. (D) High-angle annular dark-field STEM image of monolayer 1T phase MoS_2. (E) CVs of 1T phase MoS_2 nanosheet paper in 0.5 M sulphate-based electrolyte solution (scan rates = 20 mV s^{-1}). (F) Capacitance retention of 1T phase MoS_2 nanosheet paper after 5000 cycles in 0.5 M Li_2SO_4, H_2SO_4 and 1 M TEA BF_4 in acetonitrile. Copyright 2015, Macmillan Publishers. (G) Ragone plot of the best volumetric power and volumetric energy densities reported from various materials. (H) Schematic of the fabrication process and photographs of the flexible electrodes. (I) TEM image of the edge-oriented MoS_2 film. (J) High-magnification TEM image of the edge-oriented MoS_2 film. Copyright 2014, John Wiley & Sons Inc.

surface area (2630 m^2 g^{-1}).[137] Therefore, it can be a promising substrate to improve the charge-storage capacity of MoS_2-based devices. Leite *et al.*[138] developed a simple chemical route to deposit MoS_2 on reduced graphene oxide (RGO) using microwave heating and obtained a MoS_2/RGO hybrid material with MoS_2 layers covalently bonded on the surface of the RGO. The specific capacitance measured at 10 mV s^{-1} was 128 F g^{-1} for MoS_2/RGO (with 5.6 wt% MoS_2) and the corresponding energy density was 63 W h kg^{-1}. The MoS_2/RGO electrode also exhibited good cyclic stability of up to 1000 cycles with 92% of the specific capacitance retained. Generally, graphene as a soft substrate for MoS_2 can facilitate electron transport through MoS_2 nanostructures, which can provide faster ion diffusion between MoS_2 layers/electrolytes. Bissett *et al.*[139] reported the high performance of MoS_2–graphene composite membranes as supercapacitor electrodes in a symmetrical coin cell using an aqueous electrolyte. Graphene could reduce the resistivity of the electrode material and modify the morphology of the composite membrane, which significantly increased the specific capacitance of MoS_2. When the composite was synthesized with a weight ratio of 1 : 3 (MoS_2/graphene), the composite membrane achieved a high specific capacitance of ~11 mF cm^{-2} at 5 mV s^{-1}. Huang *et al.*[140] reported fabrication of a MoS_2/MWCNT composite *via* a hydrothermal method. The composite showed a specific capacitance of 452.7 F g^{-1} in 1 M Na_2SO_4 and exhibited an excellent cycle life (95.8% capacitance retention after 1000 cycles). Carbon aerogel-incorporated MoS_2 was also reported as a highly efficient supercapacitor electrode.[141] The MoS_2/carbon aerogel hybrid film electrode showed a specific capacitance of 260 F g^{-1} in Na_2SO_4 aqueous solution and exhibited good cycling stability (92.4% capacitance retention after 1500 cycles). The high surface area of these carbon materials could provide EDL capacitance in the hybrid electrode.

Besides those carbon materials, conducting polymers were also investigated for the incorporation of MoS_2. As another kind of pseudocapacitive material, conducting polymers can improve electrode conductivity and interfacial properties as well as capacitance.[142] Huang *et al.*[143] reported an *in situ* polymerization method to synthesize a polyaniline/MoS_2 nanocomposite for application in supercapacitor electrodes. The MoS_2 nanocomposite was supported by polyaniline with a high surface area, which provided a direct pathway for electron transfer. The layered nanostructure of polyaniline/MoS_2 composites provided a large surface area for ion intercalation/deintercalation, leading to a specific capacitance of 575 F g^{-1} at 1 A g^{-1}. The polyaniline/MoS_2 composite also shows an energy density of 265 W h kg^{-1} at a power density of 18.0 kW kg^{-1}. Ma *et al.*[144] reported fabrication of a polypyrrole/MoS_2 nanocomposite as a supercapacitor electrode. The polypyrrole/MoS_2 composite was synthesized through *in situ* intercalative polymerization of pyrrole in MoS_2. Electrochemical tests showed that the polypyrrole/MoS_2 electrode exhibited a high specific capacitance of 553.7 F g^{-1} in 1 M KCl aqueous solution and good cyclic performance (90% capacitance retention after 500 cycles).

4.5 Applications in sensors

In addition to applications in ESCs, MoS_2-based platforms have been also applied as sensors in different fields. According to the direct bandgap character of monolayer MoS_2, Zhang's group prepared a phototransistor based on single-layer MoS_2, which exhibited an on/off ratio of 10^3 within *ca.* 50 ms.[145] Although a response of tens of picoseconds was observed in graphene-based devices due to the ballistic carrier transport in graphene, fast carrier transport and a short photocarrier lifetime led to the recombination of photogenerated carriers.[146] Sanchez and his coworkers further optimized layered MoS_2-based ultrasensitive phototransistors.[147] The phototransistors exhibited a photoresponsivity of 880 A W^{-1}, surpassing the graphene photodetectors by a factor of 10^6. The MoS_2-based photodetector had a broad spectral range from 680 nm to 400 nm, and the photocurrent increased as the wavelength of the incident light decreased. In contrast to silicon avalanche photodiodes, low dark currents were achieved in MoS_2-based photodetectors, which resulted from the presence of a bandgap and a high degree of electrostatic control. This makes MoS_2 an ideal platform for applications in optoelectronics and field effect transistors (FETs).

FET-based detection has been applied in sensors by monitoring the change in conductance upon contact with different molecules. 2D graphene-based FET sensors provided low noise and highly sensitive detection for various molecules.[146] This inspired researchers to use MoS_2-based FETs as sensitive sensors. In view of the fact that the cleaved MoS_2 sheet was an n-type semiconductor, a MoS_2-based FET device was applied for detection of NO gas.[148] P-doping in the MoS_2 channel was induced by exposure to the electron-withdrawing NO gas, resulting in an increase in conductivity. The sensor exhibited high sensitivity toward NO, with a detection limit down to 0.8 ppm. Furthermore, a planar sensor structure consisting of a monolayer MoS_2 channel on SiO_2/Si wafers was constructed by Jonker's group (Fig. 13A).[149] The change in the conductance was monitored upon exposure to a variety of chemicals, which was measured using a lock-in amplifier in a combined probe station/gas bubbler dosing system. The conductance of monolayer MoS_2 increased abruptly with initial exposure to triethylamine (TEA) (Fig. 13B), and was much more sensitive than the multilayer MoS_2. In addition, the response and sensitivity of the MoS_2 monolayer to other chemical gases were also determined. A similar response could be observed upon exposure to acetone, although with except lower sensitivity (Fig. 13C). However, the MoS_2 sensor exhibited no measurable change in conductivity upon exposure to chemicals which are considered to be electron acceptors. Meanwhile, the application area of the MoS_2-based sensor was extended to identification of the VOC composite in the breath of patients. By applying pure MoS_2 or conjugating a ligand to the MoS_2 surface, a sensor platform was fabricated for representative VOC groups with high sensitivity, down to a concentration of 1 ppm. The sensor exhibited positive responses for oxygen-functionalized VOCs, while a MUA-conjugated MoS_2 sensor presented negative responses. The fabrication of VOC sensors provides the possibility to predict some diseases in the early stage simply by breath analysis.

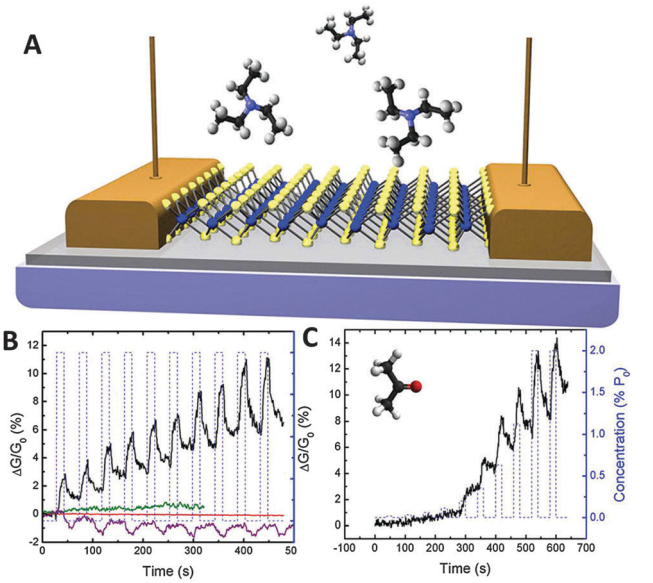

Fig. 13 (A) Schematic and image of the MoS_2 monolayer sensor: a single monolayer of MoS_2 is supported on the SiO_2/Si substrate and contacted with Au contact pads. Transient physisorption of molecules induces temporary changes in the conductivity of the monolayer channel. (B) Change in conductivity of the monolayer MoS_2 sensor channel upon exposure to a sequence of 0.002% P_0 TEA pulses (black line). The dashed blue lines show the pulse timing (15 s on/30 s off) and concentration. The solid red line shows the response to exposure of nitrogen only and serves as a control experiment. The solid green and purple lines show the response of the MoS_2 and graphene sensors to water vapor pulses (0.025% P_0), respectively. (C) Change in conductivity of the monolayer MoS_2 sensor channel upon exposure to a sequence of pulses in which the acetone concentration increases from 0.02% P_0 to 2% P_0 (black line). 2013, American Chemical Society.

Moreover, electrochemical sensors having the attributes of simplicity, low cost, ultrahigh sensitivity and selectivity have been applied for the detection of various chemicals in aqueous environments. Generally, the working mechanism of the sensors is based on electron transfer between the surface of a working electrode and a target in the electrolyte solution. Meanwhile, voltammetry, amperometry and potentiometry are the three main techniques used for the detection of aqueous chemical species. Recently, MoS_2 has been used as a sensing material for electrochemical sensors because of the superior electrochemical properties derived from its amplified edge effects and enhanced surface to volume ratios in contrast to metal oxides and conducting polymers. Additionally, some noble metals have also been anchored on the surface of these 2D TMDs to enhance the sensor signals. Huang *et al.* designed an electrochemical sensor for detection of Bisphenol A using a MoS_2 nanoflower–chitosan–Au nanoparticle modified glassy carbon electrode (GCE).[150] In the presence of bisphenol, the MoS_2-modified GCE had an anodic peak with remarkably enhanced current at a low oxidation overpotential of 0.9 V. More importantly, the stability and quantitatively reproducible analytical performance of the electrode promise to make this an excellent sensor for practical applications. Thus, it is reasonable to speculate that the formation of MoS_2 hybrids with other nanostructures may provide ideal platforms for electrochemical sensors.

Therefore, research should be carried out to improve the understanding of MoS_2 and large-scale fabrication of single-layer MoS_2 with controllable properties, thereby resulting in the fabrication of inexpensive, high-sensitivity and flexible MoS_2-based devices for practical applications in the field of sensing.

5. Conclusion and outlook

In this review, we summarized the recent progress in the development of MoS_2 nanostructures in a broad range of applications, such as energy conversion, energy storage and sensors. The discussion has focused on the optimization of structure for superior performance. We identified the key challenges facing MoS_2-based applications, and enumerated some current and emerging strategies for improving their performance.

In the pursuit of solutions for the energy crisis, theoretical studies predicted that MoS_2 could be used as an effective and lower cost substitute for the noble metals in the ESCs. In HER, the maximization of active edges and the conductivity are identified as the core issues in MoS_2-based electrocatalysts. A large number of synthetic strategies have been focused on maximizing the exposure of edge sites; phase structure tuning has also been as a potential tool for enhancing the electrical transport properties of MoS_2 which is another key factor in HER performance. To combine high carrier transport and maximum exposure of active sites, MoS_2-based composites have been prepared, and exhibited much higher activity in contrast to MoS_2 alone. Moreover, the composites have been found to be the efficient materials in the fields of MoS_2-based sensors, LIBs and supercapacitors as well.

Overall, the rich chemistry of the layered TMDs constructs an extensive platform for the study of fundamental scientific phenomena, and their versatile properties make them attractive for a wide range of practical applications. Still, there is much room for improvement in the development of TMDs with higher performance. In particular, the band structure and Fermi level tuning may be powerful tools. Thus, we should first explore the balance point in the combination of theoretical, fundamental, and performance-based studies. In addition, to enable final applications, the rate of the synthesis of large-scale and high quality MoS_2 should be accelerated. To provide solutions for the energy crisis, a number of important and exciting studies based on the tunable properties of MoS_2 and its family numbers ($MoSe_2$, WS_2, WSe_2...) will certainly emerge in the near future.

Acknowledgements

Financial support from the National Science Fund for Distinguished Young Scholars of China (Grant No. 51225805), the Funds for Creative Research Groups of China (No. 51221892), National Natural Science Foundation of China (No. 51225805, No. 51221892, and No. 21235004), National Basic Research Program of China (No. 2013CB934004), and Tsinghua University Initiative Scientific Research Program is acknowledged.

Notes and references

1 Y.-J. Wang, D. P. Wilkinson and J. Zhang, *Chem. Rev.*, 2011, **111**, 7625–7651.
2 N. G. Sahoo, Y. Pan, L. Li and S. H. Chan, *Adv. Mater.*, 2012, **24**, 4203–4210.
3 S. E. Habas, H. A. S. Platt, M. F. A. M. van Hest and D. S. Ginley, *Chem. Rev.*, 2010, **110**, 6571–6594.
4 A. Kubacka, M. Fernández-García and G. Colón, *Chem. Rev.*, 2012, **112**, 1555–1614.
5 M. Gratzel, *Nature*, 2001, **414**, 338–344.
6 H. Li, Z. Wang, L. Chen and X. Huang, *Adv. Mater.*, 2009, **21**, 4593–4607.
7 P. G. Bruce, B. Scrosati and J.-M. Tarascon, *Angew. Chem., Int. Ed.*, 2008, **47**, 2930–2946.
8 K. Naoi, W. Naoi, S. Aoyagi, J.-i. Miyamoto and T. Kamino, *Acc. Chem. Res.*, 2013, **46**, 1075–1083.
9 H. I. Karunadasa, E. Montalvo, Y. Sun, M. Majda, J. R. Long and C. J. Chang, *Science*, 2012, **335**, 698–702.
10 C. Zhu, X. Mu, P. A. van Aken, Y. Yu and J. Maier, *Angew. Chem., Int. Ed.*, 2014, **53**, 2152–2156.
11 E. Gourmelon, O. Lignier, H. Hadouda, G. Couturier, J. C. Bernède, J. Tedd, J. Pouzet and J. Salardenne, *Sol. Energy Mater. Sol. Cells*, 1997, **46**, 115–121.
12 B. Radisavljevic, A. Radenovic, J. Brivio, V. Giacometti and A. Kis, *Nat. Nanotechnol.*, 2011, **6**, 147–150.
13 M. Chhowalla, H. S. Shin, G. Eda, L.-J. Li, K. P. Loh and H. Zhang, *Nat. Chem.*, 2013, **5**, 263–275.

14 B. Hinnemann, P. G. Moses, J. Bonde, K. P. Jørgensen, J. H. Nielsen, S. Horch, I. Chorkendorff and J. K. Nørskov, *J. Am. Chem. Soc.*, 2005, **127**, 5308–5309.
15 D. Kong, H. Wang, J. J. Cha, M. Pasta, K. J. Koski, J. Yao and Y. Cui, *Nano Lett.*, 2013, **13**, 1341–1347.
16 X. Huang, Z. Zeng and H. Zhang, *Chem. Soc. Rev.*, 2013, **42**, 1934–1946.
17 W. Han, P. Yuan, Y. Fan, G. Shi, H. Liu, D. Bai and X. Bao, *J. Mater. Chem.*, 2012, **22**, 25340–25353.
18 A. B. Laursen, S. Kegnaes, S. Dahl and I. Chorkendorff, *Energy Environ. Sci.*, 2012, **5**, 5577–5591.
19 M. A. Lukowski, A. S. Daniel, F. Meng, A. Forticaux, L. Li and S. Jin, *J. Am. Chem. Soc.*, 2013, **135**, 10274–10277.
20 J. R. McKone, E. L. Warren, M. J. Bierman, S. W. Boettcher, B. S. Brunschwig, N. S. Lewis and H. B. Gray, *Energy Environ. Sci.*, 2011, **4**, 3573–3583.
21 T. F. Jaramillo, K. P. Jørgensen, J. Bonde, J. H. Nielsen, S. Horch and I. Chorkendorff, *Science*, 2007, **317**, 100–102.
22 S. Z. Butler, S. M. Hollen, L. Cao, Y. Cui, J. A. Gupta, H. R. Gutiérrez, T. F. Heinz, S. S. Hong, J. Huang, A. F. Ismach, E. Johnston-Halperin, M. Kuno, V. V. Plashnitsa, R. D. Robinson, R. S. Ruoff, S. Salahuddin, J. Shan, L. Shi, M. G. Spencer, M. Terrones, W. Windl and J. E. Goldberger, *ACS Nano*, 2013, **7**, 2898–2926.
23 K. F. Mak, K. He, J. Shan and T. F. Heinz, *Nat. Nanotechnol.*, 2012, **7**, 494–498.
24 Y. Li, H. Wang, L. Xie, Y. Liang, G. Hong and H. Dai, *J. Am. Chem. Soc.*, 2011, **133**, 7296–7299.
25 X. Hong, J. Kim, S.-F. Shi, Y. Zhang, C. Jin, Y. Sun, S. Tongay, J. Wu, Y. Zhang and F. Wang, *Nat. Nanotechnol.*, 2014, **9**, 682–686.
26 K. Roy, M. Padmanabhan, S. Goswami, T. P. Sai, G. Ramalingam, S. Raghavan and A. Ghosh, *Nat. Nanotechnol.*, 2013, **8**, 826–830.
27 Y. Gong, J. Lin, X. Wang, G. Shi, S. Lei, Z. Lin, X. Zou, G. Ye, R. Vajtai, B. I. Yakobson, H. Terrones, M. Terrones, B. K. Tay, J. Lou, S. T. Pantelides, Z. Liu, W. Zhou and P. M. Ajayan, *Nat. Mater.*, 2014, **13**, 1135–1142.
28 J. Mann, Q. Ma, P. M. Odenthal, M. Isarraraz, D. Le, E. Preciado, D. Barroso, K. Yamaguchi, G. v. S. Palacio, N. Andrew, T. Tai, M. Wurch, N. Ariana, V. Klee, S. Bobek, D. Sun, T. F. Heinz, T. S. Rahman, R. Kawakami and L. Bartels, *Adv. Mater.*, 2014, **26**, 1399–1404.
29 K. Chang and W. Chen, *Chem. Commun.*, 2011, **47**, 4252–4254.
30 H. Hwang, H. Kim and J. Cho, *Nano Lett.*, 2011, **11**, 4826–4830.
31 K. Chang, Z. Mei, T. Wang, Q. Kang, S. Ouyang and J. Ye, *ACS Nano*, 2014, **8**, 7078–7087.
32 Y. Liu, Y.-X. Yu and W.-D. Zhang, *J. Phys. Chem. C*, 2013, **117**, 12949–12957.
33 B. Cho, A. R. Kim, Y. Park, J. Yoon, Y.-J. Lee, S. Lee, T. J. Yoo, C. G. Kang, B. H. Lee, H. C. Ko, D.-H. Kim and M. G. Hahm, *ACS Appl. Mater. Interfaces*, 2015, **7**, 2952–2959.
34 D. Sarkar, W. Liu, X. Xie, A. C. Anselmo, S. Mitragotri and K. Banerjee, *ACS Nano*, 2014, **8**, 3992–4003.
35 X. Xie, D. Sarkar, W. Liu, J. Kang, O. Marinov, M. J. Deen and K. Banerjee, *ACS Nano*, 2014, **8**, 5633–5640.
36 T. Wang, H. Zhu, J. Zhuo, Z. Zhu, P. Papakonstantinou, G. Lubarsky, J. Lin and M. Li, *Anal. Chem.*, 2013, **85**, 10289–10295.
37 Y. Lin, X. Ling, L. Yu, S. Huang, A. L. Hsu, Y.-H. Lee, J. Kong, M. S. Dresselhaus and T. Palacios, *Nano Lett.*, 2014, **14**, 5569–5576.
38 X. Zhang, Z. Lai, Z. Liu, C. Tan, Y. Huang, B. Li, M. Zhao, L. Xie, W. Huang and H. Zhang, *Angew. Chem., Int. Ed.*, 2015, **54**, 5425–5428.
39 H. Li, G. Lu, Z. Yin, Q. He, H. Li, Q. Zhang and H. Zhang, *Small*, 2012, **8**, 682–686.
40 H. Li, G. Lu, Y. Wang, Z. Yin, C. Cong, Q. He, L. Wang, F. Ding, T. Yu and H. Zhang, *Small*, 2013, **9**, 1974–1981.
41 P. Joensen, R. F. Frindt and S. R. Morrison, *Mater. Res. Bull.*, 1986, **21**, 457–461.
42 Z. Zeng, T. Sun, J. Zhu, X. Huang, Z. Yin, G. Lu, Z. Fan, Q. Yan, H. H. Hng and H. Zhang, *Angew. Chem., Int. Ed.*, 2012, **51**, 9052–9056.
43 H. Wang, H. Feng and J. Li, *Small*, 2014, **10**, 2165–2181.
44 J. N. Coleman, M. Lotya, A. O'Neill, S. D. Bergin, P. J. King, U. Khan, K. Young, A. Gaucher, S. De, R. J. Smith, I. V. Shvets, S. K. Arora, G. Stanton, H.-Y. Kim, K. Lee, G. T. Kim, G. S. Duesberg, T. Hallam, J. J. Boland, J. J. Wang, J. F. Donegan, J. C. Grunlan, G. Moriarty, A. Shmeliov, R. J. Nicholls, J. M. Perkins, E. M. Grieveson, K. Theuwissen, D. W. McComb, P. D. Nellist and V. Nicolosi, *Science*, 2011, **331**, 568–571.
45 W. Zhang, J.-K. Huang, C.-H. Chen, Y.-H. Chang, Y.-J. Cheng and L.-J. Li, *Adv. Mater.*, 2013, **25**, 3456–3461.
46 H. Schmidt, S. Wang, L. Chu, M. Toh, R. Kumar, W. Zhao, A. H. C. Neto, J. Martin, S. Adam, B. Oezyilmaz and G. Eda, *Nano Lett.*, 2014, **14**, 1909–1913.
47 H. Luo, C. Xu, D. Zou, L. Wang and T. Ying, *Mater. Lett.*, 2008, **62**, 3558–3560.
48 K. S. Novoselov, D. Jiang, F. Schedin, T. J. Booth, V. V. Khotkevich, S. V. Morozov and A. K. Geim, *Proc. Natl. Acad. Sci. U. S. A.*, 2005, **102**, 10451–10453.
49 X. Liu, T. Xu, X. Wu, Z. Zhang, J. Yu, H. Qiu, J.-H. Hong, C.-H. Jin, J.-X. Li, X.-R. Wang, L.-T. Sun and W. Guo, *Nat. Commun.*, 2013, **4**, 1776.
50 S. Ghatak, A. N. Pal and A. Ghosh, *ACS Nano*, 2011, **5**, 7707–7712.
51 C. Lee, Q. Li, W. Kalb, X.-Z. Liu, H. Berger, R. W. Carpick and J. Hone, *Science*, 2010, **328**, 76–80.
52 Z. Zeng, Z. Yin, X. Huang, H. Li, Q. He, G. Lu, F. Boey and H. Zhang, *Angew. Chem., Int. Ed.*, 2011, **50**, 11093–11097.
53 A. O'Neill, U. Khan and J. N. Coleman, *Chem. Mater.*, 2012, **24**, 2414–2421.
54 J. Z. Ou, A. F. Chrimes, Y. Wang, S.-y. Tang, M. S. Strano and K. Kalantar-zadeh, *Nano Lett.*, 2014, **14**, 857–863.
55 K.-G. Zhou, N.-N. Mao, H.-X. Wang, Y. Peng and H.-L. Zhang, *Angew. Chem., Int. Ed.*, 2011, **50**, 10839–10842.
56 R. J. Smith, P. J. King, M. Lotya, C. Wirtz, U. Khan, S. De, A. O'Neill, G. S. Duesberg, J. C. Grunlan, G. Moriarty,

J. Chen, J. Wang, A. I. Minett, V. Nicolosi and J. N. Coleman, *Adv. Mater.*, 2011, **23**, 3944–3948.
57 G. Guan, S. Zhang, S. Liu, Y. Cai, M. Low, C. P. Teng, I. Y. Phang, Y. Cheng, K. L. Duei, B. M. Srinivasan, Y. Zheng, Y.-W. Zhang and M.-Y. Han, *J. Am. Chem. Soc.*, 2015, **137**, 6152–6155.
58 Q. Ji, Y. Zhang, T. Gao, Y. Zhang, D. Ma, M. Liu, Y. Chen, X. Qiao, P.-H. Tan, M. Kan, J. Feng, Q. Sun and Z. Liu, *Nano Lett.*, 2013, **13**, 3870–3877.
59 J. Shi, D. Ma, G.-F. Han, Y. Zhang, Q. Ji, T. Gao, J. Sun, X. Song, C. Li, Y. Zhang, X.-Y. Lang, Y. Zhang and Z. Liu, *ACS Nano*, 2014, **8**, 10196–10204.
60 S. Najmaei, Z. Liu, W. Zhou, X. Zou, G. Shi, S. Lei, B. I. Yakobson, J.-C. Idrobo, P. M. Ajayan and J. Lou, *Nat. Mater.*, 2013, **12**, 754–759.
61 Y.-H. Lee, X.-Q. Zhang, W. Zhang, M.-T. Chang, C.-T. Lin, K.-D. Chang, Y.-C. Yu, J. T.-W. Wang, C.-S. Chang, L.-J. Li and T.-W. Lin, *Adv. Mater.*, 2012, **24**, 2320–2325.
62 Y. Feldman, E. Wasserman, D. J. Srolovitz and R. Tenne, *Science*, 1995, **267**, 222–225.
63 L. Margulis, G. Salitra, R. Tenne and M. Talianker, *Nature*, 1993, **365**, 113–114.
64 J. Shi, D. Ma, G.-F. Han, Y. Zhang, Q. Ji, T. Gao, J. Sun, X. Song, C. Li, Y. Zhang, X.-Y. Lang, Y. Zhang and Z. Liu, *ACS Nano*, 2014, **8**, 10196–10204.
65 Y. Zhan, Z. Liu, S. Najmaei, P. M. Ajayan and J. Lou, *Small*, 2012, **8**, 966–971.
66 X. H. Chen and R. Fan, *Chem. Mater.*, 2001, **13**, 802–805.
67 Y. Yan, B. Xia, X. Ge, Z. Liu, J.-Y. Wang and X. Wang, *ACS Appl. Mater. Interfaces*, 2013, **5**, 12794–12798.
68 J. Xie, H. Zhang, S. Li, R. Wang, X. Sun, M. Zhou, J. Zhou, X. W. Lou and Y. Xie, *Adv. Mater.*, 2013, **25**, 5807–5813.
69 L. Cai, J. He, Q. Liu, T. Yao, L. Chen, W. Yan, F. Hu, Y. Jiang, Y. Zhao, T. Hu, Z. Sun and S. Wei, *J. Am. Chem. Soc.*, 2015, **137**, 2622–2627.
70 M.-R. Gao, J.-X. Liang, Y.-R. Zheng, Y.-F. Xu, J. Jiang, Q. Gao, J. Li and S.-H. Yu, *Nat. Commun.*, 2015, **6**, 5982.
71 K.-K. Liu, W. Zhang, Y.-H. Lee, Y.-C. Lin, M.-T. Chang, C. Su, C.-S. Chang, H. Li, Y. Shi, H. Zhang, C.-S. Lai and L.-J. Li, *Nano Lett.*, 2012, **12**, 1538–1544.
72 A. R. Beal, W. Y. Liang and J. C. Knights, *J. Phys. C: Solid State Phys.*, 1972, **5**, 3540–3551.
73 G. Xu, X. Wang, Y. Sun, X. Chen, J. Zheng, L. Sun, L. Jiao and J. Li, *Nano Res.*, 2015, **8**, 2946–2953.
74 D. Voiry, A. Mohite and M. Chhowalla, *Chem. Soc. Rev.*, 2015, **44**, 2702–2712.
75 D. Voiry, A. Goswami, R. Kappera, C. d. C. Castro e Silva, D. Kaplan, T. Fujita, M. Chen, T. Asefa and M. Chhowalla, *Nat. Chem.*, 2015, **7**, 45–49.
76 G. Eda, T. Fujita, H. Yamaguchi, D. Voiry, M. Chen and M. Chhowalla, *ACS Nano*, 2012, **6**, 7311–7317.
77 Y.-C. Lin, D. O. Dumcenco, Y.-S. Huang and K. Suenaga, *Nat. Nanotechnol.*, 2014, **9**, 391–396.
78 L. F. Mattheiss, *Phys. Rev. B: Solid State*, 1973, **8**, 3719–3740.
79 M. Chhowalla, H. S. Shin, G. Eda, L.-J. Li, K. P. Loh and H. Zhang, *Nat. Chem.*, 2013, **5**, 263–275.
80 A. Splendiani, L. Sun, Y. Zhang, T. Li, J. Kim, C.-Y. Chim, G. Galli and F. Wang, *Nano Lett.*, 2010, **10**, 1271–1275.
81 S. Tongay, J. Zhou, C. Ataca, K. Lo, T. S. Matthews, J. Li, J. C. Grossman and J. Wu, *Nano Lett.*, 2012, **12**, 5576–5580.
82 W. Zhao, Z. Ghorannevis, L. Chu, M. Toh, C. Kloc, P.-H. Tan and G. Eda, *ACS Nano*, 2013, **7**, 791–797.
83 J. L. Verble and T. J. Wieting, *Phys. Rev. Lett.*, 1970, **25**, 362–365.
84 C. Lee, H. Yan, L. E. Brus, T. F. Heinz, J. Hone and S. Ryu, *ACS Nano*, 2010, **4**, 2695–2700.
85 M. V. Bollinger, J. V. Lauritsen, K. W. Jacobsen, J. K. Nørskov, S. Helveg and F. Besenbacher, *Phys. Rev. Lett.*, 2001, **87**, 196803.
86 K.-K. Liu, W. Zhang, Y.-H. Lee, Y.-C. Lin, M.-T. Chang, C.-Y. Su, C.-S. Chang, H. Li, Y. Shi, H. Zhang, C.-S. Lai and L.-J. Li, *Nano Lett.*, 2012, **12**, 1538–1544.
87 Y. Shi, W. Zhou, A.-Y. Lu, W. Fang, Y.-H. Lee, A. L. Hsu, S. M. Kim, K. K. Kim, H. Y. Yang, L.-J. Li, J.-C. Idrobo and J. Kong, *Nano Lett.*, 2012, **12**, 2784–2791.
88 H. Wang, D. Kong, P. Johanes, J. J. Cha, G. Zheng, K. Yan, N. Liu and Y. Cui, *Nano Lett.*, 2013, **13**, 3426–3433.
89 R. Tenne and M. Redlich, *Chem. Soc. Rev.*, 2010, **39**, 1423–1434.
90 J. Kibsgaard, Z. Chen, B. N. Reinecke and T. F. Jaramillo, *Nat. Mater.*, 2012, **11**, 963–969.
91 D. Y. Chung, S.-K. Park, Y.-H. Chung, S.-H. Yu, D.-H. Lim, N. Jung, H. C. Ham, H.-Y. Park, Y. Piao, S. J. Yoo and Y.-E. Sung, *Nanoscale*, 2014, **6**, 2131–2136.
92 D. Voiry, H. Yamaguchi, J. Li, R. Silva, D. C. B. Alves, T. Fujita, M. Chen, T. Asefa, V. B. Shenoy, G. Eda and M. Chhowalla, *Nat. Mater.*, 2013, **12**, 850–855.
93 D. Voiry, M. Salehi, R. Silva, T. Fujita, M. Chen, T. Asefa, V. B. Shenoy, G. Eda and M. Chhowalla, *Nano Lett.*, 2013, **13**, 6222–6227.
94 J. Heising and M. G. Kanatzidis, *J. Am. Chem. Soc.*, 1999, **121**, 11720–11732.
95 M. S. Faber and S. Jin, *Energy Environ. Sci.*, 2014, **7**, 3519–3542.
96 J. Xie, J. Zhang, S. Li, F. Grote, X. Zhang, H. Zhang, R. Wang, Y. Lei, B. Pan and Y. Xie, *J. Am. Chem. Soc.*, 2013, **135**, 17881–17888.
97 D. Mocatta, G. Cohen, J. Schattner, O. Millo, E. Rabani and U. Banin, *Science*, 2011, **332**, 77–81.
98 Y. Liang, Y. Li, H. Wang, J. Zhou, J. Wang, T. Regier and H. Dai, *Nat. Mater.*, 2011, **10**, 780–786.
99 Y. Yan, B. Xia, X. Qi, H. Wang, R. Xu, J.-Y. Wang, H. Zhang and X. Wang, *Chem. Commun.*, 2013, **49**, 4884–4886.
100 C. Tsai, F. Abild-Pedersen and J. K. Nørskov, *Nano Lett.*, 2014, **14**, 1381–1387.
101 Y. Liang, Y. Li, H. Wang and H. Dai, *J. Am. Chem. Soc.*, 2013, **135**, 2013–2036.
102 D. J. Li, U. N. Maiti, J. Lim, D. S. Choi, W. J. Lee, Y. Oh, G. Y. Lee and S. O. Kim, *Nano Lett.*, 2014, **14**, 1228–1233.
103 L. Lai, J. R. Potts, D. Zhan, L. Wang, C. K. Poh, C. Tang, H. Gong, Z. Shen, J. Lin and R. S. Ruoff, *Energy Environ. Sci.*, 2012, **5**, 7936–7942.

104 H. Wang, Z. Lu, D. Kong, J. Sun, T. M. Hymel and Y. Cui, *ACS Nano*, 2014, **8**, 4940–4947.
105 D. Merki and X. Hu, *Energy Environ. Sci.*, 2011, **4**, 3878–3888.
106 R. Parsons, *Trans. Faraday Soc.*, 1958, **54**, 1053–1063.
107 J. Kibsgaard and T. F. Jaramillo, *Angew. Chem., Int. Ed.*, 2014, **53**, 14433–14437.
108 X. Zhang, F. Meng, S. Mao, Q. Ding, M. J. Shearer, M. S. Faber, J. Chen, R. J. Hamers and S. Jin, *Energy Environ. Sci.*, 2015, **8**, 862–868.
109 S. Kanda, T. Akita, M. Fujishima and H. Tada, *J. Colloid Interface Sci.*, 2011, **354**, 607–610.
110 X. Zong, H. Yan, G. Wu, G. Ma, F. Wen, L. Wang and C. Li, *J. Am. Chem. Soc.*, 2008, **130**, 7176–7177.
111 Q. Ding, F. Meng, C. R. English, M. Cabán-Acevedo, M. J. Shearer, D. Liang, A. S. Daniel, R. J. Hamers and S. Jin, *J. Am. Chem. Soc.*, 2014, **136**, 8504–8507.
112 G. Shirane, S. Hoshino and K. Suzuki, *Phys. Rev.*, 1950, **80**, 1105–1106.
113 Q. M. Zhang, V. Bharti and X. Zhao, *Science*, 1998, **280**, 2101–2104.
114 C. Lee, X. Wei, J. W. Kysar and J. Hone, *Science*, 2008, **321**, 385–388.
115 W. Wu, L. Wang, Y. Li, F. Zhang, L. Lin, S. Niu, D. Chenet, X. Zhang, Y. Hao, T. F. Heinz, J. Hone and Z. L. Wang, *Nature*, 2014, **514**, 470–474.
116 T. Stephenson, Z. Li, B. Olsen and D. Mitlin, *Energy Environ. Sci.*, 2014, **7**, 209–231.
117 Q. Wang and J. Li, *J. Phys. Chem. C*, 2007, **111**, 1675–1682.
118 M. R. Palacin, *Chem. Soc. Rev.*, 2009, **38**, 2565–2575.
119 G. Du, Z. Guo, S. Wang, R. Zeng, Z. Chen and H. Liu, *Chem. Commun.*, 2010, **46**, 1106–1108.
120 X. Zhou, L.-J. Wan and Y.-G. Guo, *Chem. Commun.*, 2013, **49**, 1838–1840.
121 K. Chang and W. Chen, *ACS Nano*, 2011, **5**, 4720–4728.
122 X. Xu, Z. Fan, X. Yu, S. Ding, D. Yu and X. W. Lou, *Adv. Energy Mater.*, 2014, **4**, 1400902.
123 X. Xu, Z. Fan, S. Ding, D. Yu and Y. Du, *Nanoscale*, 2014, **6**, 5245–5250.
124 H. Liu, D. Su, R. Zhou, B. Sun, G. Wang and S. Z. Qiao, *Adv. Energy Mater.*, 2012, **2**, 970–975.
125 H. Yu, C. Zhu, K. Zhang, Y. Chen, C. Li, P. Gao, P. Yang and Q. Ouyang, *J. Mater. Chem. A*, 2014, **2**, 4551–4557.
126 B. E. Conway, *Electrochemical Supercapacitors: Scientific Fundamentals and Technological Applications*, Springer, 1999.
127 V. Augustyn, J. Come, M. A. Lowe, J. W. Kim, P. L. Taberna, S. H. Tolbert, H. D. Abruna, P. Simon and B. Dunn, *Nat. Mater.*, 2013, **12**, 518–522.
128 J. M. Soon and K. P. Loh, *Electrochem. Solid-State Lett.*, 2007, **10**, A250–A254.
129 M. Acerce, D. Voiry and M. Chhowalla, *Nat. Nanotechnol.*, 2015, **10**, 313–318.
130 Y. Yang, H. Fei, G. Ruan, C. Xiang and J. M. Tour, *Adv. Mater.*, 2014, **26**, 8163–8168.
131 L. Cao, S. Yang, W. Gao, Z. Liu, Y. Gong, L. Ma, G. Shi, S. Lei, Y. Zhang, S. Zhang, R. Vajtai and P. M. Ajayan, *Small*, 2013, **9**, 2905–2910.
132 X. Wang, J. Ding, S. Yao, X. Wu, Q. Feng, Z. Wang and B. Geng, *J. Mater. Chem. A*, 2014, **2**, 15958–15963.
133 L. Ma, L.-M. Xu, X.-P. Zhou and X.-Y. Xu, *Mater. Lett.*, 2014, **132**, 291–294.
134 P. Ilanchezhiyan, G. M. Kumar and T. W. Kang, *J. Alloys Compd.*, 2015, **634**, 104–108.
135 M. S. Javed, S. Dai, M. Wang, D. Guo, L. Chen, X. Wang, C. Hu and Y. Xi, *J. Power Sources*, 2015, **285**, 63–69.
136 Q. Lu, J. G. Chen and J. Q. Xiao, *Angew. Chem.*, 2013, **52**, 1882–1889.
137 Y. Zhu, S. Murali, W. Cai, X. Li, J. W. Suk, J. R. Potts and R. S. Ruoff, *Adv. Mater.*, 2010, **22**, 3906–3924.
138 E. G. da Silveira Firmiano, A. C. Rabelo, C. J. Dalmaschio, A. N. Pinheiro, E. C. Pereira, W. H. Schreiner and E. R. Leite, *Adv. Energy Mater.*, 2014, **4**, 1301380.
139 M. A. Bissett, I. A. Kinloch and R. A. W. Dryfe, *ACS Appl. Mater. Interfaces*, 2015, **7**, 17388–17398.
140 K.-J. Huang, L. Wang, J.-Z. Zhang, L.-L. Wang and Y.-P. Mo, *Energy*, 2014, **67**, 234–240.
141 K.-J. Huang, L. Wang, J.-Z. Zhang and K. Xing, *J. Electroanal. Chem.*, 2015, **752**, 33–40.
142 Y. Zhao, B. Liu, L. Pan and G. Yu, *Energy Environ. Sci.*, 2013, **6**, 2856–2870.
143 K.-J. Huang, L. Wang, Y.-J. Liu, H.-B. Wang, Y.-M. Liu and L.-L. Wang, *Electrochim. Acta*, 2013, **109**, 587–594.
144 G. Ma, H. Peng, J. Mu, H. Huang, X. Zhou and Z. Lei, *J. Power Sources*, 2013, **229**, 72–78.
145 Z. Yin, H. Li, H. Li, L. Jiang, Y. Shi, Y. Sun, G. Lu, Q. Zhang, X. Chen and H. Zhang, *ACS Nano*, 2012, **6**, 74–80.
146 F. Xia, T. Mueller, Y.-m. Lin, A. Valdes-Garcia and P. Avouris, *Nat. Nanotechnol.*, 2009, **4**, 839–843.
147 O. Lopez-Sanchez, D. Lembke, M. Kayci, A. Radenovic and A. Kis, *Nat. Nanotechnol.*, 2013, **8**, 497–501.
148 H. Li, Z. Yin, Q. He, H. Li, X. Huang, G. Lu, D. W. H. Fam, A. I. Y. Tok, Q. Zhang and H. Zhang, *Small*, 2012, **8**, 63–67.
149 F. K. Perkins, A. L. Friedman, E. Cobas, P. M. Campbell, G. G. Jernigan and B. T. Jonker, *Nano Lett.*, 2013, **13**, 668–673.
150 K.-J. Huang, Y.-J. Liu, Y.-M. Liu and L.-L. Wang, *J. Hazard. Mater.*, 2014, **276**, 207–215.